

Structure of high-redshift galaxies in cosmological simulations

Xi Meng¹ , Oleg Y. Gnedin¹  and Hui Li² 

¹Department of Astronomy, University of Michigan, Ann Arbor, MI 48109, USA

²Department of Physics, Kavli Institute for Astrophysics and Space Research, MIT, Cambridge, MA 02139, USA

Accepted XXX. Received YYY; in original form ZZZ

ABSTRACT

We investigate the structure of galaxies formed in a suite of high-resolution cosmological simulations. Consistent with observations of high-redshift galaxies, our simulated galaxies show irregular, prolate shapes with thick stellar disks, which are dominated by turbulent motions instead of rotation. Yet molecular gas and young stars are restricted to relatively thin disks. We examine the accuracy of applying the Toomre linear stability analysis to predict the location and amount of gas available for star formation. We find that the Toomre criterion still works for these irregular galaxies, after correcting for multiple gas and stellar components: the Q parameter in H₂ rich regions is in the range 0.5 – 1, remarkably close to unity. Due to the violent stellar feedback from supernovae and strong turbulent motions, young stars and molecular gas are not always spatially associated. Neither the Q map nor the H₂ surface density map coincide with recent star formation exactly. We argue that the Toomre criterion is a better indicator of future star formation than a single H₂ surface density threshold because of the smaller dynamic range of Q . The depletion time of molecular gas is below 1 Gyr on kpc scale, but with large scatter. Centering the aperture on density peaks of gas/young stars systematically biases the depletion time to larger/smaller values and increases the scatter.

Key words: galaxies: formation — galaxies: high redshift — galaxies: kinematics and dynamics — galaxies: star formation — galaxies: structure

1 INTRODUCTION

Recent analytical models of star formation (SF) in galaxies (e.g., Dekel et al. 2009; Vollmer & Leroy 2011; Kruijssen & Longmore 2014; Krumholz et al. 2018) have used the Toomre criterion $Q \lesssim 1$ to identify regions of dense gas in disk galaxies that should collapse and form stars. The original Toomre analysis (Toomre 1964) considers stability of an isothermal gas layer to linear axisymmetric perturbations in regular, thin, axisymmetric disks. These conditions are not strictly satisfied even in many galaxies at low redshift, and are certainly violated in clumpy, turbulent disk galaxies at high redshift. Without invoking the Toomre criterion, however, it is difficult to construct predictive models that could help interpret observations of galaxies at $z \gtrsim 2$ that are expected from powerful oncoming and future facilities. In this paper we test the validity of the Toomre analysis for turbulent irregular galaxies using new state-of-the-art simulations of galaxy formation.

Deep HST-UDF observations indicate that normal spi-

ral galaxies appear only at redshifts $z < 1.5$ (Elmegreen & Elmegreen 2014). At higher redshifts galaxies tend to have thick stellar disks fragmented into dense stellar clumps (e.g., Genzel et al. 2010; Elmegreen et al. 2017). These galaxies have kinematics dominated by turbulent motions and show comparable amounts of molecular gas and stars (Tacconi et al. 2013). In some cases enhanced spatial resolution afforded by gravitational lensing reveals that the locations molecular gas and UV emission from young stars are spatially decoupled on sub-kpc scales (Dessauges-Zavadsky et al. 2017). Measurements of the Toomre Q parameter find values exceeding unity for ionized H α gas but giant clumps appear to be unstable with $Q < 1$ (Genzel et al. 2014). Similarly, in a study of low-redshift analogues of turbulent disk galaxies Fisher et al. (2017) find that large H α clumps exist only in regions with $Q < 1$.

Numerical simulations have also studied stability of galactic disks. Li et al. (2005, 2006) calculated the Toomre Q for a combination of collisional gas and collisionless stars in isolated disk simulations. Ceverino et al. (2010) and Inoue et al. (2016) used cosmological simulations of clumpy high-redshift galaxies and found values of $Q > 1$ in large

* E-mail: xim@umich.edu

parts of the disks. More recent isolated galaxy simulations show that stellar clumps fragment further on smaller sub-kpc scales, below the characteristic Toomre mass (Tamburro et al. 2015). These simulations of high-redshift galaxies show significantly irregular structure of the disks due to fast gas accretion and stellar feedback. The kinematics of the interstellar medium includes strong turbulent motions on all scales.

Given this complexity, is it correct to apply the Toomre analysis to select regions undergoing gravitational collapse and star formation? How well can we predict the amount of star-forming gas and star formation rate (SFR) in high-redshift galaxies?

Our goal is to estimate the accuracy of applying the Toomre criterion and Toomre fragmentation mass. Using a recent suite of cosmological simulations of Milky Way-type galaxies, we verify the validity of the Toomre analysis. We argue that the Q parameter is a better predictor of the star formation sites than simply the molecular gas density, because it covers a smaller dynamic range. We also study the depletion time of cold gas as a function of spatial scale and, in agreement with previous non-cosmological studies, show that the two commonly used approaches (gas-centered and star-centered) give very different estimates on ~ 100 pc scales but converge on kpc scale.

We describe the simulations used for this analysis and the spatial and kinematic structure of simulated galaxies in Section 2. We apply the Toomre analysis and calculate maps of the Q parameter in Section 3. In Section 4 we study the depletion time of cold molecular gas on different spatial scales. We discuss the implications of our results for modeling galactic star formation in Section 5 and present our conclusions in Section 6.

2 STRUCTURE OF HIGH REDSHIFT GALAXIES

2.1 Simulation Suite

We use a suite of cosmological simulations described in Li et al. (2017, 2018). These simulations were run with the Adaptive Refinement Tree (ART) code (Kravtsov et al. 1997; Kravtsov 1999, 2003; Rudd et al. 2008) in a periodic box of 4 comoving Mpc. All runs start with the same initial conditions but use different sub-grid model parameters of star formation and stellar feedback. The initial conditions were selected to produce a main halo with total mass $M_{200} \approx 10^{12} M_{\odot}$ at $z = 0$, similar to that of the Milky Way. The ART code uses adaptive mesh refinement to increase spatial resolution in the dense galactic regions. The lowest resolution level is set by the root grid, which in these runs was 128^3 cells. This sets the dark matter particle mass $m_{\text{DM}} = 1.05 \times 10^6 M_{\odot}$. The refinement strategy is quasi-Lagrangian, which keeps cell mass within a narrow range. The finest refinement level is chosen so that the physical size of gas cells at that level is between 3 and 6 pc. This required increasing the number of additional refinement levels gradually with time, from 9 levels at $z > 9$ to 10, 11, and 12 refinement levels at $z \approx 9, 4, 1.5$, respectively.

The simulations include three-dimensional radiative transfer using the Optically Thin Variable Eddington Tensor

approximation (Gnedin & Abel 2001) of ionizing and ultraviolet radiation from stars (Gnedin 2014) and the extragalactic UV background (Haardt & Madau 2001), non-equilibrium chemical network that deals with ionization states of hydrogen and helium, and phenomenological molecular hydrogen formation and destruction (Gnedin & Kravtsov 2011). The simulations also incorporate a subgrid-scale (SGS) model for unresolved gas turbulence (Schmidt et al. 2014; Semenov et al. 2016). The star formation is implemented with a new method that follows the formation of individual star clusters. In this continuous cluster formation (CCF) algorithm (Li et al. 2017, 2018) each star particle represents a star cluster that forms at a local density peak and grows mass via accretion within a spherical region of fixed physical size, until the feedback of young stars terminates the growth of the star cluster.

In addition to the early radiative and stellar wind feedback, the simulations include a supernova (SN) remnant feedback model (Martizzi et al. 2015; Semenov et al. 2016). As the SN remnant model was calibrated by simulations of isolated SN explosion, rather than multiple SNe that appear in star clusters, its momentum feedback is underestimated. In addition, some momentum is lost due to advection errors as the SN shell moves across the simulation grid. Cosmic rays accelerated by the SN remnant could also boost the momentum deposition (Diesing & Caprioli 2018). To compensate for these effects, the momentum feedback of the SN remnant model is boosted by a factor f_{boost} . The default value $f_{\text{boost}} = 5$ is chosen to match the star formation history expected from the abundance matching method, but the simulation suite contains also runs with different f_{boost} .

In this paper we focus on several runs with different local star formation efficiency ϵ_{ff} and SN momentum boost factor f_{boost} . Table 1 contains basic information of these simulations. The number after "SFE" in the names corresponds to the percentage of local ϵ_{ff} . In SFEturb run ϵ_{ff} is variable and turbulence-dependent (as implemented by Semenov et al. 2016). SFE50-SNR3 run is a weaker feedback run, with the lower SN boost factor $f_{\text{boost}} = 3$. All other runs have $f_{\text{boost}} = 5$. We focus on the main galaxy in the last available output of each run and list their masses and sizes in Table 1. For run SFE200 we analyze the snapshot at $z = 1.78$ (same as for SFE10 run), because at the last output ($z = 1.44$) the main galaxy is experiencing a major merger and its morphology is strongly perturbed.

2.2 Surface density profiles

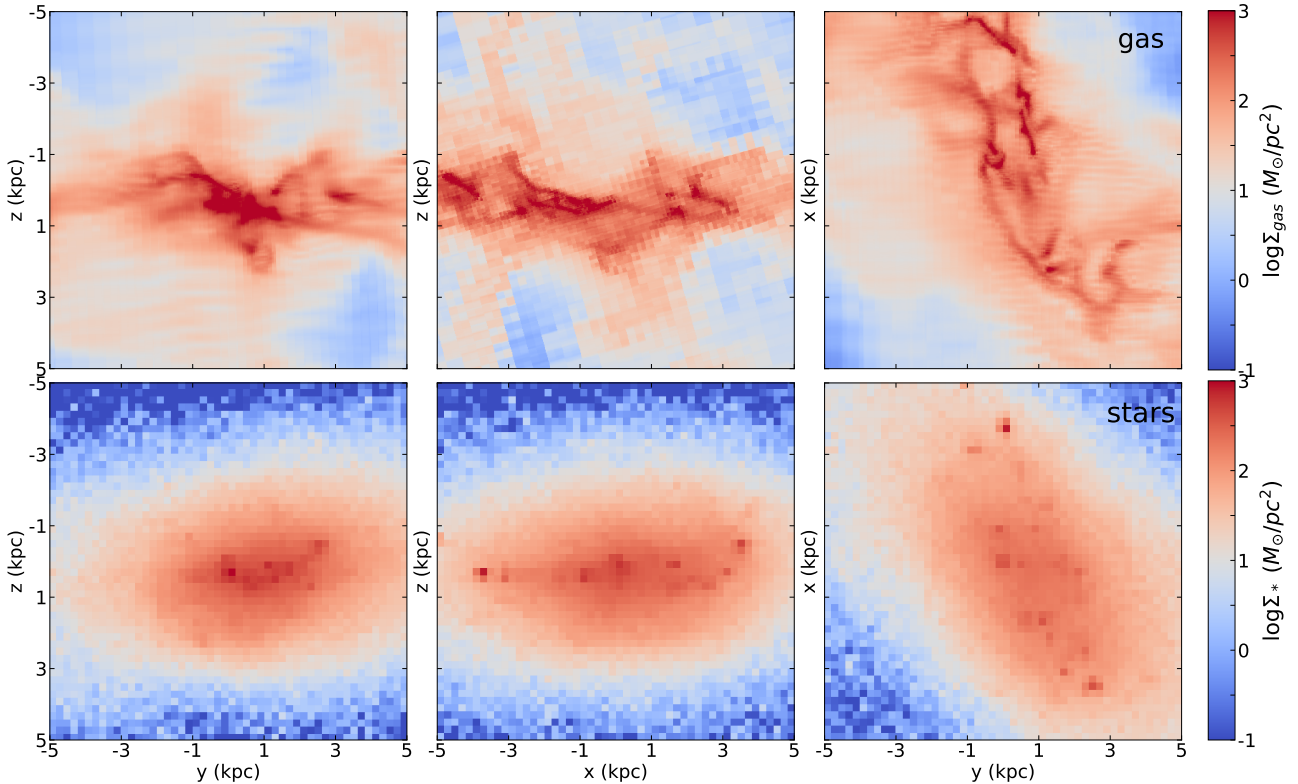
To study the surface density profile of the simulated galaxies, we need to determine the center of a galaxy and orientation of the projection plane. We define the galaxy center to be at the location of maximum stellar density, which is found iteratively using smaller and smaller smoothing kernels in Brown et al. (2018). To determine the disk orientation, we examined several alternative definitions based on the angular momentum of neutral gas and the principle axes of the tensor of inertia of gas and stars.

We use the following definition of the inertia tensor (also called "shape tensor" in Zemp et al. 2011)

$$\mathbf{I} \equiv \sum_{k,i,j} M_k r_{k,i} r_{k,j} \mathbf{e}_i \otimes \mathbf{e}_j$$

Table 1. Global properties of the main galaxy

| Run | z | $M_h (M_\odot)$ | $M_*(M_\odot)$ | $M_{\text{HI+H}_2} (M_\odot)$ | $M_{\text{H}_2} (M_\odot)$ | $R_{\text{vir}} (\text{kpc})$ | $R_{h,*} (\text{kpc})$ | $R_{h,\text{HI+H}_2} (\text{kpc})$ | $R_{h,\text{H}_2} (\text{kpc})$ |
|------------|------|-----------------------|-----------------------|-------------------------------|----------------------------|-------------------------------|------------------------|------------------------------------|---------------------------------|
| SFE200 | 1.78 | 2.37×10^{11} | 4.06×10^9 | 2.65×10^9 | 1.77×10^8 | 67.9 | 2.6 | 3.2 | 2.3 |
| SFE100 | 1.50 | 4.36×10^{11} | 8.19×10^9 | 7.23×10^9 | 8.54×10^8 | 91.5 | 2.7 | 4.7 | 2.2 |
| SFE50 | 1.50 | 4.35×10^{11} | 7.13×10^9 | 8.35×10^9 | 7.47×10^8 | 91.5 | 4.0 | 8.6 | 2.8 |
| SFE10 | 1.78 | 2.50×10^{11} | 6.46×10^9 | 4.98×10^9 | 1.15×10^9 | 69.0 | 2.4 | 3.6 | 2.3 |
| SFETurb | 2.85 | 1.21×10^{11} | 2.44×10^9 | 2.78×10^9 | 2.59×10^8 | 39.2 | 2.2 | 4.0 | 2.1 |
| SFE50-SNR3 | 1.98 | 2.40×10^{11} | 1.37×10^{10} | 3.29×10^9 | 1.88×10^9 | 63.5 | 0.7 | 1.3 | 0.9 |

**Figure 1.** Density projection of all gas (upper panels) and stars (lower panels) along three principle axes given by the tensor of inertia of neutral gas, for run SFE50 at $z = 1.5$. Z -coordinate corresponds to the minor axis. Thus the right panels are "face-on" while the left and middle panels are "edge-on" views. The projection depth is ± 5 kpc.

where M_k is the mass of k -th stellar particle or gas cell, $r_{k,i}$ are its coordinates in the galactocentric reference frame ($i = 1, 2, 3$), and \mathbf{e}_i are the three unit vectors of the coordinate axes. The tensor can be diagonalized by a rotation matrix, to calculate the principle moments of inertia $I_1 \geq I_2 \geq I_3$. From these we calculate the axis ratios $b/a = (I_2/I_1)^{1/2}$ and $c/a = (I_3/I_1)^{1/2}$. The orientation of the disk is given by the eigenvector corresponding to the smallest eigenvalue.

We find that the angular momentum of neutral (HI + H₂) gas enclosed within a sphere of a given radius can suddenly change direction between $0.1 R_{\text{vir}}$ and $0.3 R_{\text{vir}}$ in some runs. For example, in SFE50 run it changes by 82° , and in SFETurb run by 52° , while in the other runs it remains stable within 10° . At large radii the gas typically falls along cosmic filaments, whereas closer to the center mergers of galactic clumps can significantly perturb the disk orientation. Since most of the stars and neutral gas in the simulated galaxies are located within $0.1 R_{\text{vir}}$, the inner angular

momentum is more relevant to the disk formation. Within $0.1 R_{\text{vir}}$ the direction of the gas angular momentum is consistent to better than 20° for all runs. The direction of angular momentum of molecular H₂ gas generally follows that of the neutral gas, to better than 16° . The scale of $0.1 R_{\text{vir}}$ corresponds to 4–9 kpc (Table 1); it varies from galaxy to galaxy because of the different redshift of the final available output.

Next we consider the principal axes of the shape tensor for neutral gas and stars, calculated with the $0.1 R_{\text{vir}}$ radius sphere. Their orientation can deviate from the angular momentum of neutral gas by as much as 36° in SFETurb run and 24° in SFE50 run. For the other runs they are within $\approx 10^\circ$. The moments of inertia calculated separately for the gas and stars generally agree with each other.

Although we first expected that the cold gas would settle into a thin disk and its angular momentum would be the best indicator of the rotation plane, we found by experimentation that the shape tensor gives a more consistent defini-

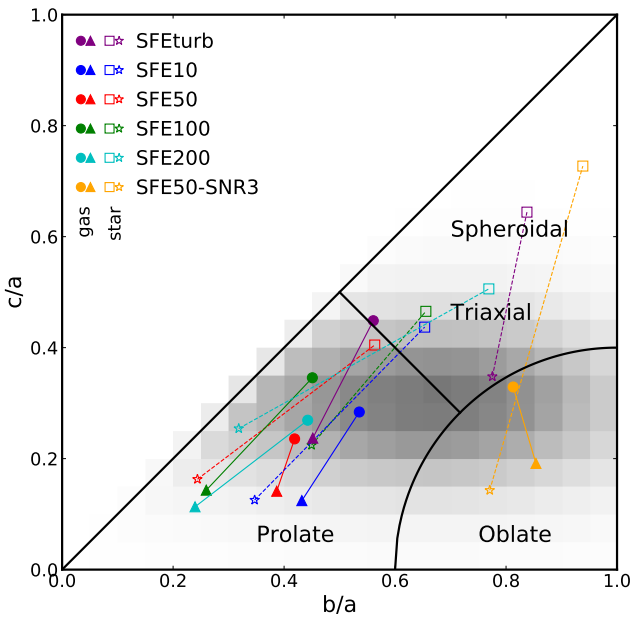


Figure 2. Axis ratios of all gas (filled circles) and molecular gas (filled triangles), and all stars (open squares) and young stars (asterisks) for different runs. The parameter space of the axis ratios b/a and c/a is divided into three parts to distinguish shapes of an ellipsoid, following the definition in [Zhang et al. \(2018\)](#) and [van der Wel et al. \(2014\)](#). The gray shades show the observed distribution of axis ratios for stars in the high redshift galaxies of similar mass range to our simulated galaxies ([Zhang et al. 2018](#)).

tion of the disk. Therefore, we choose to use the gas shape tensor to define the disk plane. Similarly, [Garrison-Kimmel et al. \(2018\)](#) used the inertia tensor of stars to define the disk orientation in their analysis of FIRE-2 simulations.

Figure 1 shows examples of the density map of gas and stars projected along the three principle axes. The stellar distribution is strongly puffed up in the vertical direction and elongated in the disk plane. The axis ratios from the shape tensor show that, except for SFE50-SNR3 run, our simulated galaxies are not thin, axisymmetric disks. The axis ratios c/a and b/a for stars are generally around 0.4 and 0.6, respectively (for SFEturb run they are around 0.65 and 0.85), while the axis ratios for neutral gas are around 0.3 and 0.5 (for SFE200 run they are around 0.5 and 0.8). Axis ratios vary from galaxy to galaxy, but except for SFE50-SNR3 run (which has $b/a = 0.9$ for stars and $b/a = 0.8$ for molecular gas) they all indicate non-axisymmetric, triaxial shapes for both stars and molecular gas. This can be seen in the right panels of Figure 1, where the face-on view of the galaxy is not axisymmetric.

[van der Wel et al. \(2014\)](#) intuitively defined galaxy shapes to be oblate, prolate, or spheroidal based on the axis ratios. Here we adopt their definition and plot the axis ratios for the gas and stars in our simulated galaxies in Figure 2. Two runs stand out from the rest. The SFE50-SNR3 run has weaker feedback, which produces a more regular disk and shows features qualitatively different from all the other runs. The SFEturb output is at an earlier epoch, which could be the cause of its different axis ratios of stars from the other runs with the fiducial feedback strength.

As pointed out by [Zhang et al. \(2018\)](#), the "spheroidal"

regime also contains triaxial shapes and is better named as "spheroidal or triaxial". [Zhang et al. \(2018\)](#) assumed that the intrinsic shapes of galaxies are triaxial ellipsoids and fit ellipses with the same b/a axis ratios to isophote contours (instead of using the tensor of inertia). Then they used a model to reconstruct the three-dimensional shape based on the observed two-dimensional axis ratios for galaxies in the multi-wavelength CANDELS survey. They used data in wavelengths that are as close as possible to 4600Å in rest-frame, which better traces the distribution of young stars. We show in gray shades in Figure 2 their modeled axis ratio distribution for the redshift bin $1.5 < z < 2.0$ and mass bin $9.5 < \log M_*/M_\odot < 10$, which are closest to our simulated galaxies. Compared to the observations, the distribution of stars in our galaxies is typically rounder and thicker, extending from mildly prolate to triaxial to spheroidal regimes. The shape of the gas is significantly more flattened, falling into the prolate regime. [Ceverino et al. \(2015\)](#) and [Tomassetti et al. \(2016\)](#) also find that the shapes of $z \approx 1 - 3$ galaxies in their simulations tend to be triaxial or prolate.

However, the shapes of molecular gas and young stars are much more flattened ($c/a = 0.1 - 0.2$) and elongated ($b/a < 0.5$). Since the number of young star particles is not large and their distribution is clumpy (except for SFE50-SNR3 run) it is easy for young stars and molecular gas to display an elongated, prolate configuration. The shapes of young stars and molecular gas are similar, because the stars form out of molecular gas. As the galaxy evolves and interacts with other galaxies, these newly formed stars leave their formation sites and settle into a more spheroidal configuration.

Current observations suggest that galaxies transform from clumpy, thick disks at $z \gtrsim 1.5$ (e.g., [Elmegreen et al. 2017](#)) to regular, spiral structures at low redshift as galactic disks become less turbulent ([Elmegreen & Elmegreen 2014](#)). During this process galaxy shapes transit from prolate to oblate ([Zhang et al. 2018](#)), while the gas fraction decreases ([Dessauges-Zavadsky et al. 2017](#)). [Shibuya et al. \(2016\)](#) found that the fraction of clumpy galaxies increases at $z \gtrsim 2$, peaks at $z \approx 1 - 2$, and decreases at $z \lesssim 1$. This also indicates that galaxies transit from irregular morphology at high redshift to more regular, disk shapes at relatively low redshift.

Figure 3 shows an example of the surface density profile of stars and gas in one galaxy. Stars dominate over gas near the center but have similar density in the range of radii $0.4 < R < 3$ kpc. The gas density decreases less steeply with radius and begins to dominate over stars at larger radii. Since some of our galaxies have spheroidal shapes, we chose a large projection depth of 5 kpc to capture most of the stars and gas extending above the disk plane. Because of such a deep projection the molecular gas does not dominate in any cylindrical shell, but still reaches very high column density, $10 - 50 M_\odot \text{ pc}^{-2}$, in the inner few kpc. Outside $R = 5$ kpc the H_2 density is low. When we calculate the Toomre Q parameter in later sections, we focus on the square region of ± 5 kpc from the center of the galaxy, which contains most of the star-forming molecular gas. The total gas and stellar surface densities in this region are comparable. The density profile of young stars formed within the last 50 Myr is quite irregular and does not directly follow the distribution

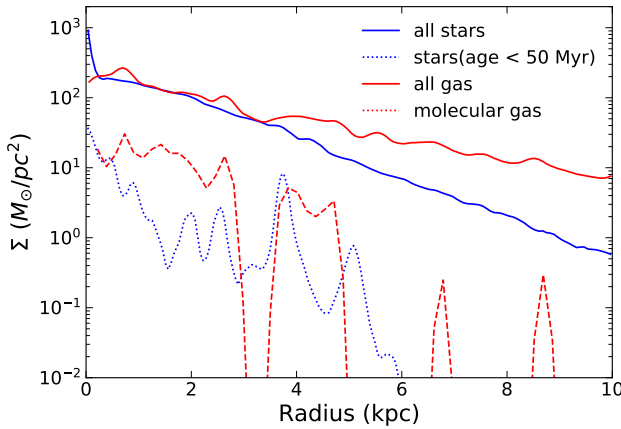


Figure 3. An example of the surface density profiles of gas and stars in cylindrical shells in run SFE50. The projection depth is ± 5 kpc.

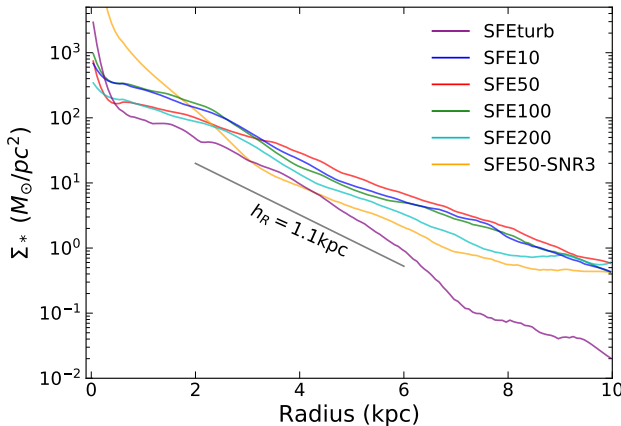


Figure 4. Comparison of the stellar surface density profiles for all six runs. Gray line corresponds to an exponential disk with the scale length of 1.1 kpc.

of molecular gas. We return to this point in the discussion of density maps.

Figure 4 compares the stellar profiles of galaxies in different runs. Even though our disks are thick, all of them can still be fit reasonably well by an exponential disk model with the scale length $h_R = 1.1 \pm 0.1$ kpc, in the radial range 2–6 kpc. The only exception is run SFE50 that has $h_R \approx 1.5$ kpc. Since the gas density profiles are shallower, formation of new stars over time would gradually increase the stellar scale length.

Interestingly, observations of clumpy galaxies at $z \approx 1-2$ (e.g., [Shibuya et al. 2016](#)) find surface brightness profiles with the Sérsic index of $n \approx 1$, corresponding to an exponential disk. For example, massive ($M_* \sim 10^{9.6} M_\odot$) star-forming galaxies at $1 < z < 3$ in the ZFOURGE survey can be fit by $n \approx 1.2$ and an effective radius of $R_e \approx 2$ kpc ([Papovich et al. 2015](#); [Forrest et al. 2018](#)). This is very close to the effective radii we obtain for our galaxies: $R_e \approx 1.68 h_R \approx 1.8$ kpc. Thus the stellar density profiles of our simulated galaxies are typical of star-forming galaxies at these intermediate redshifts.

2.3 Velocity dispersion profiles

The kinematics of the interstellar medium in the simulated galaxies is shaped to a large extent by turbulent flows. The ART code models the injection of unresolved (subgrid scale) turbulence by SN explosions, as well as turbulent cascade from resolved scales. Even though these turbulent motions decay on a dynamical timescale, they still play an important role in distributing the SN energy over the neighboring cells in actively star-forming galaxies.

Figure 5 shows kinematic profiles of the molecular gas in all six galaxies. Using the previously defined center and orientation of the disk, the rotation curve is calculated in linearly spaced cylindrical shells of 200 pc in width. The SGS turbulence is averaged over the cells falling into the cylindrical shell. The resolved velocity dispersion σ_{cell} is the residual motion of cells, after subtracting the mean rotation velocity. Both dispersions are calculated in three dimensions, weighted by H_2 gas mass. When averaged over the cylindrical shells, the resolved dispersion dominates over the unresolved SGS turbulence. The resolved dispersion is comparable to the rotation velocity by amplitude and typically anticorrelates in radius.

Two runs stand out from the general trend. The weaker feedback run SFE50-SNR3 forms a massive bulge, which leads to the sharp rise of the circular velocity at the center. The striking difference with the parallel run SFE50 with the same ϵ_{ff} , where the boost factor is only $5/3$ times larger, may seem surprising. In the inner few kpc the rotation velocities differ by more than a factor of two. A likely cause of such a difference is in the unstable nature of formation of dense stellar clumps. If a dense bulge happens to begin forming, as was the case in run SFE50-SNR3, then stellar feedback is insufficient to halt its growth until most of the inner gas is converted into stars. In the other case when momentum feedback is always sufficiently strong, massive clumps do not form and subsequent feedback succeeds in regulating star formation. The other run that shows a rising rotation velocity towards the center is SFEturb. The last available output for this run is at a higher redshift than the rest and the magnitude of the velocity increase is relatively small. It is difficult to predict whether this increase will persist to later epochs or conform to the other runs.

The turbulent flows of H_2 gas are highly supersonic. The 3D turbulent velocities reach $100 - 150 \text{ km s}^{-1}$ and violently stir the gas clouds in the disk. These flows are responsible for the thick structure of the gaseous disks of all our simulated galaxies. They also create significant vertical motion of the gas clouds.

3 TOOMRE ANALYSIS

The local stability criterion, first derived by [Safronov \(1960\)](#) and [Toomre \(1964\)](#) and reviewed in [Toomre \(1977\)](#), has been commonly used to identify star-forming regions in regular disk galaxies. For a gaseous disk, the Q parameter is defined as:

$$Q = \frac{\sigma \kappa}{\pi G \Sigma}, \quad (1)$$

where κ is the epicycle frequency, σ is the velocity dispersion, and Σ is the surface mass density. A self-gravitating disk is

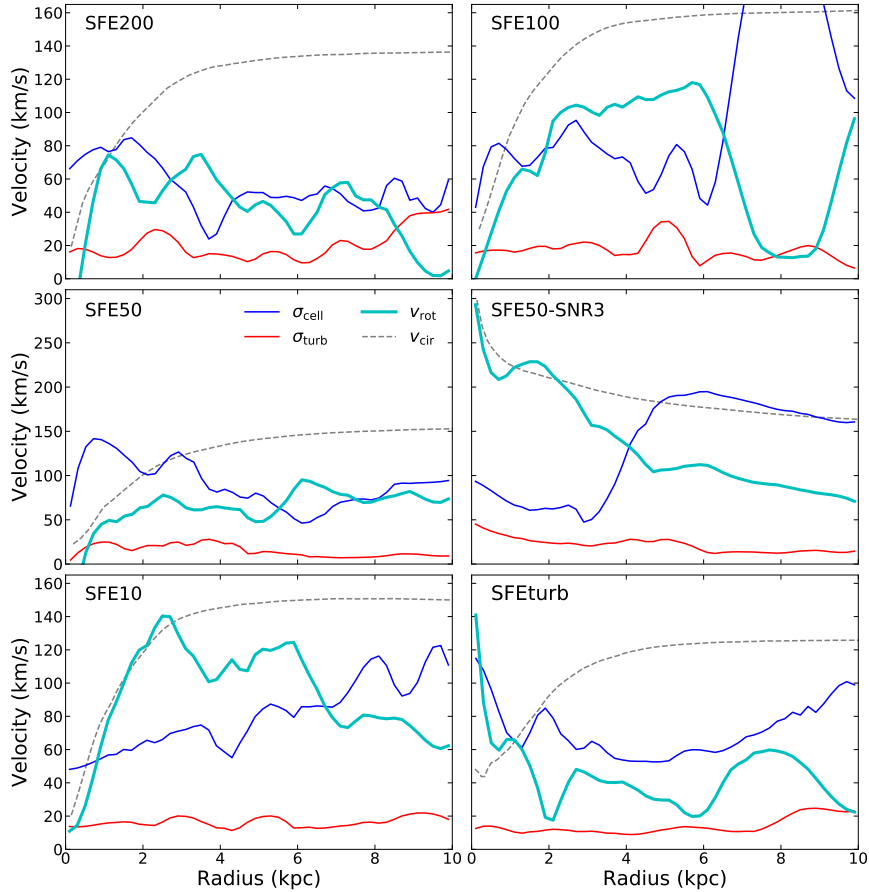


Figure 5. Kinematics of the molecular gas in the simulated galaxies, calculated in cylindrical shells: rotation velocity (cyan), subgrid-scale turbulence (red), resolved turbulence (blue). Grey dashed lines show the circular velocity profile.

stable to axisymmetric perturbations on scale λ if

$$Q > 2 \left(\frac{\lambda}{\lambda_{\text{crit}}} - \frac{\lambda^2}{\lambda_{\text{crit}}^2} \right)^{1/2}, \quad (2)$$

where λ_{crit} is the largest unstable wavelength for a zero-pressure ($\sigma = 0$) disk:

$$\lambda_{\text{crit}} \equiv \frac{4\pi^2 G \Sigma}{\kappa^2}.$$

The disk with $Q > 1$ is stable on all perturbation scales λ , but even smaller Q can indicate stability for $\lambda < \frac{1}{2}\lambda_{\text{crit}}$ (Binney & Tremaine 2008).

The wavelength of the fastest growing perturbation is not λ_{crit} but instead is given by (e.g., Nelson 2006)

$$\lambda_T \equiv \frac{2\sigma^2}{G\Sigma} = \lambda_{\text{crit}} \frac{Q^2}{2}. \quad (3)$$

It is a two-dimensional analogue of the Jeans wavelength.

The amount of gas contained within a circle of diameter λ_T is an expected mass that would collapse into a self-gravitating object, called the Toomre mass:

$$M_T \equiv \frac{\pi}{4} \lambda_T^2 \Sigma = \frac{\pi \sigma^4}{G^2 \Sigma}. \quad (4)$$

In some recent work (e.g., Reina-Campos & Kruijssen 2017;

Pfeffer et al. 2018), the Toomre mass was defined alternatively as the mass within λ_{crit} :

$$\tilde{M}_T \equiv \frac{\pi}{4} \lambda_{\text{crit}}^2 \Sigma = \frac{4\pi^5 G^2 \Sigma^3}{\kappa^4}. \quad (5)$$

The two definitions are related by

$$M_T = \tilde{M}_T \frac{Q^4}{4}.$$

For dense clumps with $Q < 1$, the alternative \tilde{M}_T can significantly overestimate the Toomre mass.

The original Toomre criterion applies to a fully gaseous disk. Real galaxies, and our simulated galaxies, contain gas, stars, and dark matter. While the dark matter has much larger velocity dispersion and does not significantly affect disk stability, stars have velocity dispersion comparable to gas and contribute additional gravitational force. Different velocity dispersions, and the corresponding different scale-heights above the disk plane, of the stellar and gaseous components mean that they affect the stability criterion in a more complicated way. Rafikov (2001) presents a detailed analysis of the stability of multi-component disks and provides a modified criterion:

$$\frac{1}{Q_R} = \max_k \left\{ \frac{1}{Q_*} \frac{2(1 - e^{-q^2} I_0(q^2))}{q} + \frac{1}{Q_g} \frac{2q\xi}{1 + q^2\xi^2} \right\} \quad (6)$$

where $q \equiv k\sigma_*/\kappa$, $\xi \equiv \sigma_g/\sigma_*$, I_0 is modified Bessel function of the first kind, and Q_* and Q_g are the separate parameters for stars and gas. The maximum is taken over values of the perturbation wavenumber $k = 2\pi/\lambda$. This criterion has been adopted in some simulations of galactic disks (e.g., Li et al. 2005).

Romeo & Wiegert (2011) and Romeo & Falstad (2013) suggest a simplified version of the modified Q parameter and show that it reasonably accurately reproduces Rafikov's criterion. The modified parameter for N components of the matter distribution is

$$Q_N = \left(\sum_{i=1}^N Q_i^{-1} \frac{2\sigma_m \sigma_i}{\sigma_m^2 + \sigma_i^2} \right)^{-1} \quad (7)$$

where Q_i are the separate parameters for each component:

$$Q_i \equiv \frac{\sigma_i \kappa}{\pi G \Sigma_i} \quad (8)$$

and σ_m is the velocity dispersion of the component with the lowest Q_i . The ratio of dispersions in equation (7) acts as a weighting factor that reduces the contribution of the other components with $\sigma_i \neq \sigma_m$. They also suggest additional correction to account for the thickness of different components. This correction is small and we do not use it in our analysis for clarity, but we denote their full formalism for the Toomre parameter as Q_{RW} .

Romeo & Falstad (2013) show that their definition of Q_N with $N = 2$ can accurately approximate Rafikov's criterion. The definition of Q_2 was adopted, for example, in the model of Krumholz et al. (2018). To examine this approximation we calculated and compared the values of Q_R and Q_2 for our galaxies, and found that indeed they agree to better than 5%. The reason for such a close match can be understood as follows. If $Q_g < Q_*$, then the maximum of equation (6) is reached when $q\xi = 1$, and the weighting factors before Q_g are unity for both expressions (Q_R and Q_2) while the weighting factors before Q_* evaluate to be within 6% of each other. If instead $Q_g > Q_*$, then the maximum of equation (6) is reached when $q = 1$, and the weighting factors before Q_g are the same while the weighting factors before Q_* are within 7% of each other. Thus in general the two expressions Q_R and Q_2 differ by no more than a few percent.

For the calculation of Q in our simulations we use equation (7) and consider three components: molecular gas (H_2 multiplied by 1.32 to account for helium within molecular clouds), atomic gas (HI plus HeI), and stars.

The wavelengths λ_{crit} and λ_T can be evaluated using the modified surface density:

$$\Sigma_{\text{eff}} \equiv \sum_{i=1}^N \Sigma_i \frac{2\sigma_m^2}{\sigma_m^2 + \sigma_i^2} \quad (9)$$

as

$$\lambda_{\text{crit}} = \frac{4\pi^2 G \Sigma_{\text{eff}}}{\kappa^2}, \quad \lambda_T = \frac{2\sigma_m^2}{G \Sigma_{\text{eff}}} \quad (10)$$

If the velocity dispersions of any two components are equal, their surface densities can be effectively combined. For example, if the dispersions of atomic and molecular gas are the same, $\sigma_{\text{HI}} = \sigma_{H_2} = \sigma_g$, then their Q_i parameters can

be combined into one

$$Q_g = (Q_{\text{HI}}^{-1} + Q_{H_2}^{-1})^{-1} = \frac{\sigma_g \kappa}{\pi G (\Sigma_{\text{HI}} + \Sigma_{H_2})}.$$

Analogously, if stars have the same velocity dispersion as the gas, their surface density can be added to the sum in the denominator. For example, Orr et al. (2018) included the sum of the gas and stars to obtain the total mass surface density, $\Sigma = \Sigma_g + \Sigma_*$, in their analysis of the FIRE simulations.

Using the simulation outputs at the last available epoch, we calculate projected maps of Q -values in square patches of physical length $L = 0.2$ kpc. The orientation of the patches is aligned with the disk plane, and the projection is along the direction perpendicular to the disk.

The size L is chosen to contain many gas cells for sufficient averaging, such that numerical discreteness does not affect the conclusions. The size of individual cells containing most of the neutral gas varies from about 50 to 100 pc at redshift $z = 1.5$. These cells are not at the highest level of refinement but dominate the gas mass. Therefore, we restrict the square patches to be no smaller than 200 pc.

Below we describe the calculation of the three variables determining the Q parameter: epicycle frequency, surface density, and velocity dispersion.

3.1 Epicycle frequency

For an axisymmetric disk with near-circular orbits (e.g., Binney & Tremaine 2008)

$$\kappa^2 = \kappa_R^2 \equiv \frac{2\bar{V}^2}{R^2} \left(1 + \frac{d \ln \bar{V}}{d \ln R} \right) \quad (11)$$

where \bar{V} is the average azimuthal velocity. We approximate it by a spherically-symmetric expression for the circular velocity:

$$V_c(R) \equiv \left(\frac{GM(R)}{R} \right)^{1/2}.$$

The actual circular velocity for a razor-thin exponential disk is given by the Bessel functions, but the difference is only $\sim 10\%$, which is below other approximations necessary for our analysis. In the limit of a flat rotation curve, $V_c = \text{const}$, and

$$\kappa^2 = \kappa_c^2 \equiv \frac{2V_c^2}{R^2}. \quad (12)$$

We define separate variables κ_R and κ_c to refer to these commonly used approximations.

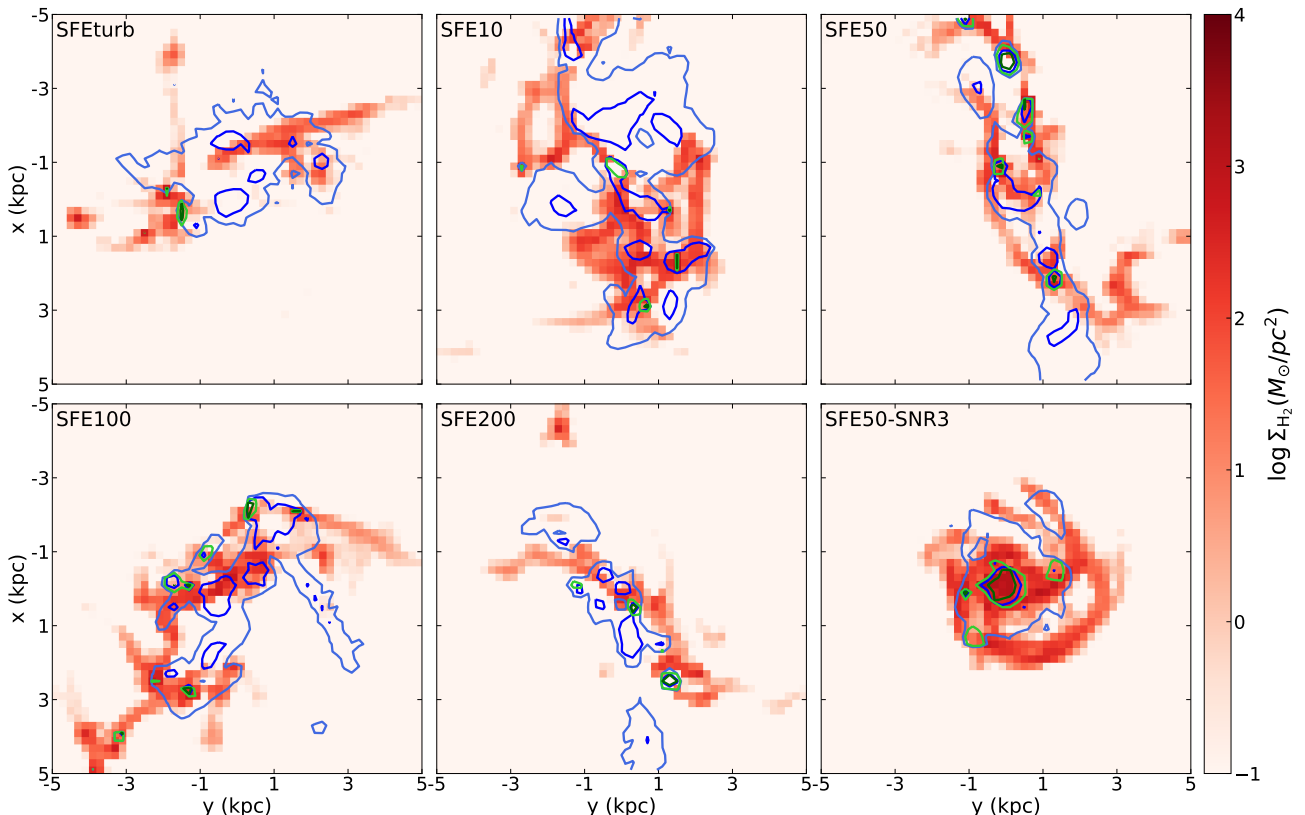
Our simulated galaxies have much smaller and irregular rotation pattern because of additional pressure support provided by turbulent motions, as shown in Figure 5, and therefore we do not expect these approximations to hold. Since the epicycle expansion is done around the mean azimuthal velocity, a more appropriate quantity is the actual rotation velocity $\bar{V} = V_{\text{rot}}$. To verify the accuracy of calculation of κ , we also evaluated the expression

$$\kappa^2 = \kappa_{\phi}^2 \equiv \frac{2V_{\text{rot}}^2}{R^2} \left(1 + \frac{d \ln V_{\text{rot}}}{d \ln R} \right). \quad (13)$$

Table 2 shows the distributions of ratios of κ given by equations (11–13). The epicycle frequencies are calculated in axisymmetric cylindrical shells of width $L = 200$ pc. As

Table 2. Accuracy of calculation of κ in various approximations

| Run | κ_c/κ_R 25-50-75% range | κ_ϕ/κ_R 25-50-75% range | κ_T/κ_R 25-50-75% range |
|------------|--|---|--|
| SFE200 | 0.79 - 0.84 - 0.94 | 0.46 - 0.57 - 0.76 | 0.60 - 0.86 - 1.17 |
| SFE100 | 0.78 - 0.82 - 0.92 | 0.57 - 0.66 - 0.79 | 0.61 - 0.84 - 1.13 |
| SFE50 | 0.74 - 0.81 - 0.96 | 0.42 - 0.52 - 0.73 | 0.61 - 0.89 - 1.21 |
| SFE10 | 0.75 - 0.86 - 0.96 | 0.61 - 0.89 - 1.07 | 0.60 - 0.90 - 1.26 |
| SFETurb | 0.75 - 0.85 - 1.03 | 0.27 - 0.62 - 1.14 | 0.58 - 0.86 - 1.19 |
| SFE50-SNR3 | 1.03 - 1.09 - 1.13 | 0.58 - 0.74 - 0.96 | 0.49 - 0.76 - 1.11 |

**Figure 6.** Map of H₂ surface density with projection thickness of ± 2 kpc. Blue contours enclose 80% and 99% of mass of young stars formed in last 50 Myr. Green contours enclose the same mass fractions of young stars formed only in last 10 Myr.

expected, the median κ_c is consistently lower than κ_R by $\sim 15\%$ because the circular velocity curves are still increasing in the range of radii we consider, $R < 5$ kpc. However, the difference is small.

The values calculated directly from the rotation velocity have a larger spread from κ_R , by $\sim 30\%$ in the median. The interquartile range of the distribution of κ_ϕ/κ_R is also wider, extending from 0.3 to 1.1. However, despite this significant scatter from shell to shell, the overall good accuracy of calculation of κ using the simple approximation of equation (11) is surprising. It validates our analysis of the Q parameter to better than a factor of two. For the distributions of Q parameter described below the epicycle frequency is calculated in cylindrical shells within the disk plane using equation (11), except in maps shown in Figure 7 where we use equation (12) to avoid visual artifacts.

Inoue et al. (2016) used their simulations of high-redshift galaxies to compare the calculation of κ using the circular velocity V_c and the actual rotation velocity V_{rot} . In agreement with our results, they find that the latter gives somewhat lower values, but the difference is small. They also note that the rotation velocity can decrease with radius suddenly and lead to $\kappa^2 < 0$ in some shells in the outer parts of the galaxies.

In addition to the above approximations, we evaluate another expression for the epicycle frequency suggested by Pfeffer et al. (2018):

$$\kappa^2 = \kappa_T^2 \equiv - \sum \lambda_i - \lambda_1, \quad (14)$$

where λ_i are the eigenvalues of the tidal tensor around the patch. The maximum eigenvalue is $\lambda_1 \geq \lambda_2, \lambda_3$. We calculate the tidal tensor on the uniform grid of 200 pc patches and

evaluate the ratio of κ_T/κ_R on these patches, instead of the cylindrical shells as for the other axisymmetric definitions of κ . The ratio κ_T/κ_R is similar to κ_c/κ_R but with larger scatter. The absolute values of κ_R are similar to those in Fig. A1 of Pfeffer et al. (2018): κ_R decreases from around 200 Gyr^{-1} in inner 1 kpc to $\sim 30 \text{ Gyr}^{-1}$ at $R = 5 \text{ kpc}$, for all runs except SFE50-SNR3.

Having determined the epicycle frequency, we now calculate the corresponding Toomre mass. We use patches of 200 pc, taking Σ to be the gas surface density projected over ± 2 kpc. Then we average M_T and \tilde{M}_T (equations 4–5) in linearly-spaced cylindrical shells. Our values of M_T generally increase with radius and vary from $10^{8.2}$ to $10^{10.6} M_\odot$ (interquartile range) in the patches with $M_{\text{H}_2} > 10^6 M_\odot$ (see Section 3.4 for justification of this threshold). However, \tilde{M}_T is systematically higher; it ranges from $10^{8.6}$ to $10^{11} M_\odot$ for the same patches. This is several orders of magnitude larger than the values found by Pfeffer et al. (2018), mainly because the gas surface density in our simulations is about an order of magnitude larger.

Note that Tamburello et al. (2015) account for non-linear growth of perturbations in collapsing clumps and find that the actual fragmentation mass is lower than M_T by a factor of several. Subsequent dynamics of collapsed clumps may also affect their mass because of merging and agglomeration with other clumps. We do not investigate the distribution of clump masses in this paper but plan to do it in follow-up work.

3.2 Surface density

We calculate the surface densities of all components by projecting over a column of thickness ± 2 kpc around the disk plane. This thickness was chosen to contain most (about 80%) of the gas and stars. Only in SFE200 run such a column contains 70% of the mass. To account for 80% of the mass in that run we would need to integrate within ± 3 kpc, but this difference is not essential to our analysis and we chose to keep the column thickness the same for all runs.

In most patches the gas dominates the surface density. The median ratio Σ_*/Σ_g is in the range 0.7–0.9 for most runs. The two exceptions are SFE10 with $\Sigma_*/\Sigma_g \approx 1$ and SFE50-SNR3 with $\Sigma_*/\Sigma_g \approx 2$. Most of the gas near the disk is atomic and some is ionized. Below we investigate specifically the distribution of molecular H_2 gas, which is directly linked to star formation.

Figure 6 compares the maps of molecular gas density with star formation rate density. To calculate the star formation rate in a large patch of a galaxy within a given interval of time, we need to take into account a finite duration of formation of cluster particles in our CCF algorithm (Li et al. 2018). At the very beginning of the formation episode of each particle, the formation rate is low. Then as particle mass rises, the gas accretion rate increases and the star formation rate picks up, until stellar feedback halts the accretion. The variable τ_{ave} approximately corresponds to the peak time of formation rate. Therefore, we take the star particle “zero age” to be the moment when it has gone through one τ_{ave} after the creation. The typical values are $\tau_{\text{ave}} \sim 1–2 \text{ Myr}$.

Surprisingly, Figure 6 shows that for the majority of patches the regions of high H_2 density *do not* coincide with the regions of high SFR density. It is because strong stel-

lar feedback quickly heats and removes the gas from star forming regions. This becomes an important point in the calculation of the depletion time in Section 4.

Observations of high-redshift galaxies (e.g., Daddi et al. 2010; Tacconi et al. 2013; Dessauges-Zavadsky et al. 2017) provide an analogous comparison of CO and radio continuum maps with optical, UV, and IR images. Observed emission from molecular gas and young stars is generally in the same place, but they do not coincide exactly. Other simulation results also show decoupled gas and SFR maps. For example, in the FIRE simulations, which use $\epsilon_{\text{eff}} = 100\%$, Oklopčić et al. (2017) find that gas clumps coincide with instantaneous SFR maps fairly well, but start to decouple from the SFR averaged over 10 Myr. The map of SFR averaged over 100 Myr shows that gas clumps do not trace the SFR peaks at all. This is similar to our results, where SF averaged over 10 Myr is located near the peaks of molecular gas, while SF averaged over 50 Myr correlates less well with the H_2 map. Most of the molecular gas is not participating in star formation at any given time.

3.3 Velocity dispersion

The full velocity dispersion of gas includes three components: the sound speed within a cell c_s , the subgrid scale turbulence (SGS; unresolved velocity dispersion) within a cell σ_T , and velocity differences between neighbor cells (resolved velocity dispersion) σ_{cell} :

$$\sigma_g^2 = c_s^2 + \sigma_T^2 + \sigma_{\text{cell}}^2.$$

Using gas mass M_k in a cell k (see two versions below), we calculate the mass-weighted average of each component for the cells within a given patch:

$$\begin{aligned} c_s^2 &= \frac{\sum_k M_k c_{s,k}^2}{\sum_k M_k} \\ \sigma_T^2 &= \frac{2 \sum_k E_{\text{turb},k}}{\sum_k M_k} \\ \sigma_{\text{cell}}^2 &= \sum_{i=r,\phi,z} \left[\frac{\sum_k v_{i,k}^2 M_k}{\sum_k M_k} - \left(\frac{\sum_k v_{i,k} M_k}{\sum_k M_k} \right)^2 \right]. \end{aligned} \quad (15)$$

Here \mathbf{v}_k is the velocity of cell k in the galacto-centric reference frame, and $E_{\text{turb},k}$ is the energy in subgrid-scale turbulence in cell k , which is directly calculated in the simulation.

The goal of Toomre analysis is to identify regions of the ISM that are unstable to collapse and star formation. Which parts of the ISM are directly observable depends on the detection method. Radio observations of CO and HCN transitions probe dense molecular gas, while 21-cm line technique detects atomic hydrogen gas. To facilitate comparison with both types of observations, we consider two versions of the Q parameter, which differ only in the weighting of the velocities. In one version the sound speed and the resolved velocity dispersion are weighted by the mass of molecular gas, $M_k = M_{\text{H}_2}$, while in the other they are weighted by the mass of total neutral gas, $M_k = M_{\text{HI+H}_2}$. In the expression for the SGS turbulence, M_k is always the total gas mass. For most of our analysis we use the result of weighting by the H_2 mass; it is therefore implied by default. Only when we discuss the distribution of neutral gas, we use the HI+H_2 mass weighting for consistency.

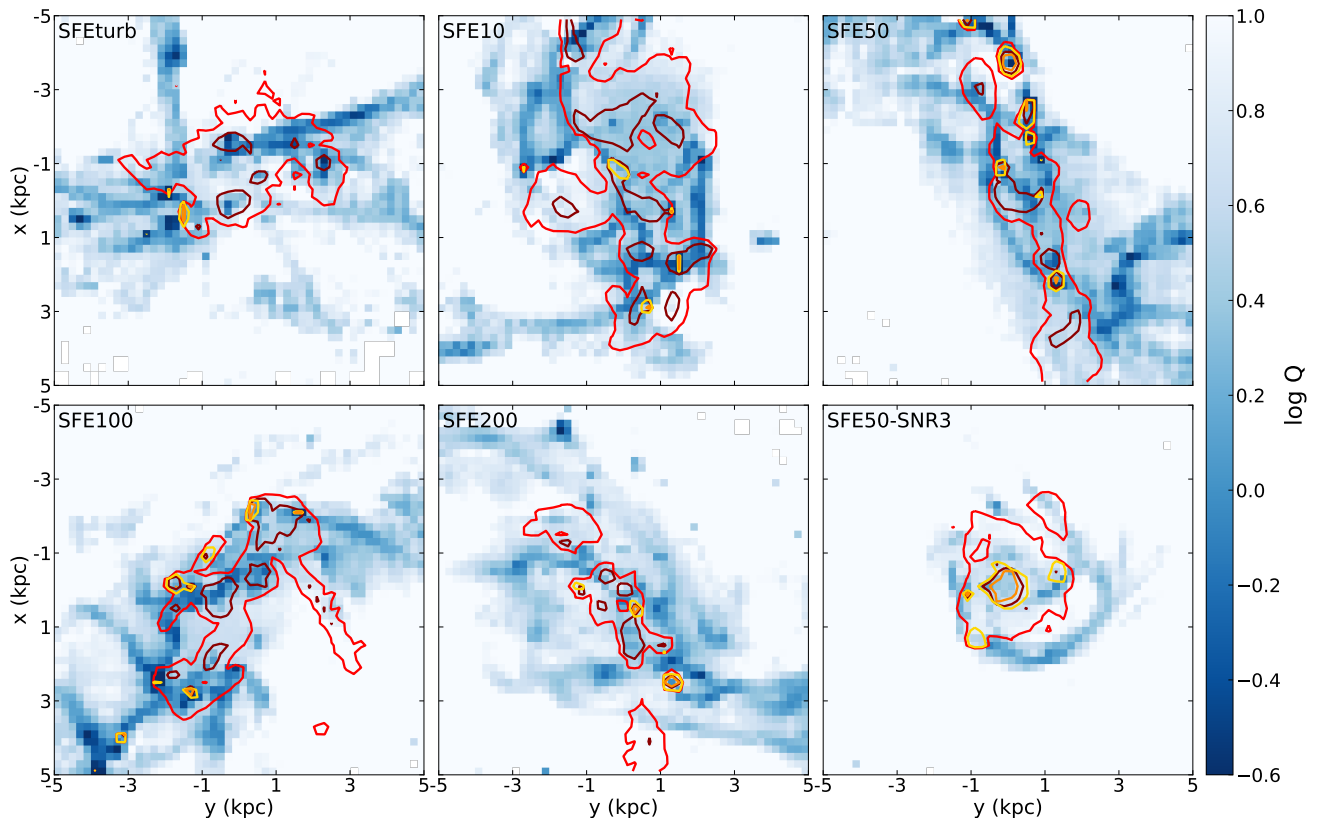


Figure 7. Map of the Q parameter in all six runs, at the last available output. Contours in red show the surface density of stars younger than 50 Myr enclosing 80% and 99% of the mass of these stars. Yellow contours enclose the same mass fractions of young stars formed only in last 10 Myr. The values of Q are calculated using the κ_c definition to avoid visual artifacts.

We take the sum over all cells in a given square patch, projected over ± 0.8 kpc. We chose this smaller projection length than for the surface density to capture most of the molecular gas while avoiding the contamination by ionized gas that could skew the measurement of the sound speed. This choice also limits the resolved velocity dispersion. The column ± 0.8 kpc contains over 90% of H_2 mass in all runs except SFEturb (which contains 80%).

Within patches of $L = 0.2$ kpc the SGS turbulence dispersion is typically larger than the resolved dispersion. The median ratio $\sigma_{\text{cell}}/\sigma_T \approx 0.6$, when σ_{cell} is H_2 mass weighted. This situation is different from the azimuthal averages shown in Figure 5, where σ_{cell} is the tangential velocity dispersion of cells in a cylindrical shell. Here instead we compute σ_{cell} using the actual local mean velocity in a patch. This reduces the residual dispersion substantially.

The velocity dispersion of stars is calculated simply as inter-particle dispersion, analogously to σ_{cell} but weighted by stellar mass. In most patches (over 75%), the stellar dispersion dominates over the gas dispersion. The median ratio $\sigma_g/\sigma_* \approx 0.4$ for the molecular H_2 gas and 0.5 for the neutral $H\text{I} + H_2$ gas.

3.4 Distribution of the Q parameter

Figure 7 shows projected maps of the Q parameter and compares them with the star formation rate density. The maps of Q generally follow the maps of gas density but pick out sharper features, such as spiral arms or filaments reaching to the galactic center. The dynamic range of Q is significantly reduced relative to that of the molecular gas surface density, which makes Q a useful predictor of future star-forming regions.

An example of the weak feedback run (bottom right panel) illustrates that some high-density regions may not be unstable because of a steep potential well and high velocity dispersion. Thus a simple density threshold would not correctly pick gas patches that are unstable to gravitational collapse.

In Figure 8 we show the cumulative distribution of Q , weighted by the mass of molecular (left panel) and all neutral hydrogen (right panel). That is, the left panel shows the fraction

$$\frac{M_{H_2}(< Q)}{M_{H_2}},$$

and analogously for $H\text{I} + H_2$ in the right panel. The weaker feedback run SFE50-SNR3 shows a very different distribu-

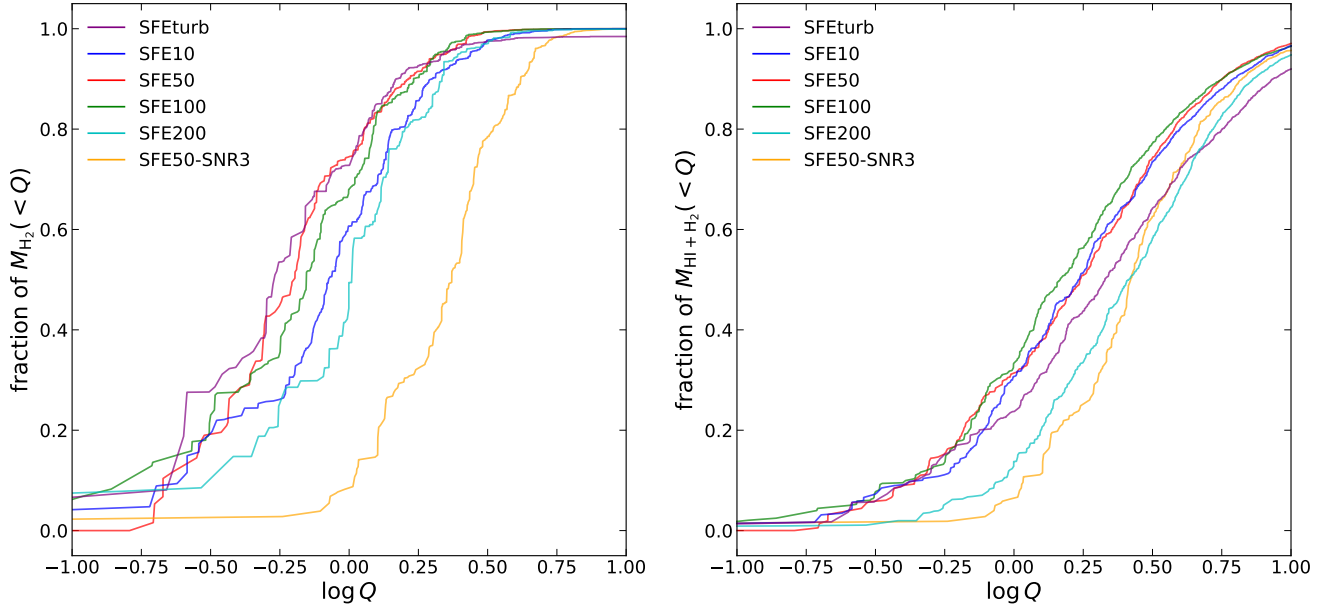


Figure 8. Cumulative distribution of the molecular H_2 (left) and neutral $\text{HI} + \text{H}_2$ (right) gas mass within ± 2 kpc as a function of Q . The velocity dispersion used to calculate Q for the right panel is weighted by the $\text{HI} + \text{H}_2$ mass for consistency. The epicyclic frequency is calculated using the κ_R definition.

tion, but all other runs with the same feedback strength show consistent results. The cumulative H_2 masses are rising sharply around the median values $Q \approx 0.5 - 1.0$. These medians are remarkably close to unity, given the many approximations in our calculation of the Q parameter and the irregular structure of these high-redshift galaxies. It also suggests that majority of the molecular gas is in the marginally stable dynamical state, which may indicate self-regulation of star formation by stellar feedback.

The distribution of neutral gas mass is shifted systematically towards higher values of $Q \approx 1.5 - 2.6$. The difference is mainly because the H_2 weighting selects regions of higher surface density and slightly lower velocity dispersion, both of which reduce Q .

The Toomre analysis indicates that there is a threshold at $Q \lesssim 1$ to distinguish the unstable regions of the disk. It is given by equation (2) that depends on the ratio of the perturbation scale to the largest unstable wavelength. To test the applicability of this analysis to the simulated galaxies, we calculated the largest unstable wavelength λ_{crit} on the patches that are capable of forming stellar particles. Because of the minimum adopted mass of stellar particles in the simulations ($\sim 10^3 M_\odot$), patches with insufficient H_2 mass are unable to produce even a single particle. This is a numerical resolution limitation and therefore, such patches should not be included in our analysis. In fact, the patch size is much larger than the size of star-forming regions adopted in our runs (~ 5 pc) and so the limiting mass should be significantly larger than the minimum particle mass. Accounting also for the low star formation efficiency in some of the simulations, we set the threshold H_2 mass at $10^6 M_\odot$. Experimentation with lower values ($10^4 - 10^5 M_\odot$) showed that the median λ_{crit} decreases as the threshold decreases, by $\approx 1 - 2$ kpc. However, we choose the larger threshold value because it leads

Table 3. Distribution of λ_{crit} and λ_T in patches of $L = 0.2$ kpc

| Run | λ_{crit} (kpc) 25-50-75% range | λ_T (kpc) 25-50-75% range |
|------------|--|--------------------------------------|
| SFE200 | 2.3 - 5.1 - 11.8 | 2.1 - 3.4 - 6.7 |
| SFE100 | 3.4 - 6.4 - 16.0 | 1.5 - 2.5 - 4.7 |
| SFE50 | 4.8 - 7.6 - 15.6 | 1.5 - 2.9 - 7.2 |
| SFE10 | 2.8 - 4.2 - 6.2 | 1.4 - 2.2 - 5.1 |
| SFEturb | 3.1 - 4.8 - 10.2 | 0.9 - 1.3 - 2.6 |
| SFE50-SNR3 | 1.1 - 1.6 - 2.5 | 3.0 - 5.9 - 11.7 |

to a more reliable calculation of the depletion time in the next section.

Table 3 shows the cumulative distributions of λ_{crit} for patches of 0.2 kpc on the side with H_2 mass above $10^6 M_\odot$. The critical wavelength is quite large, between 4 and 8 kpc in the median for all stronger feedback runs. Such large values are caused mainly by the high surface density of gas and stars in these high-redshift galaxies.

The values of the Toomre wavelength λ_T are systematically lower and range between 1 – 3 kpc in the median. SFE50-SNR3 run is again an exception because of its higher Q values. The relation between the two wavelengths, given by equation (3), is still valid even for the multi-component definition of the Q parameter.

In Figure 9 we compare the median values of Q for all the runs with the expected relation given by equation (2). We adopt the patch size as the perturbation wavelength λ . Because of large values of the critical wavelength, the ratio $\lambda/\lambda_{\text{crit}}$ is only a few percent. The median Q are all above the expected relation, yet within a factor of two from it. The lower quartile range values approach the analytical relation. We should not expect an exact match because of the approx-

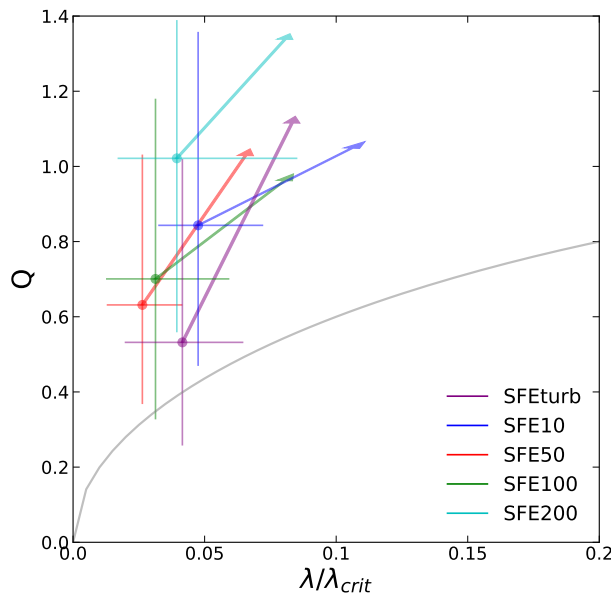


Figure 9. Median values of Q for patch size $L = 0.2$ kpc. Error-bars show the interquartile ranges in both axes. Distribution of Q is weighted by H_2 mass. Distribution of λ_{crit} is obtained for patches with $M_{H_2} > 10^6 M_\odot$ to exclude regions unable to produce stellar particles in the simulations. We take the perturbation wavelength λ to be equal the patch size L . Arrows point in the direction of change of the medians for both variables when the patch size is increased to $L = 0.4$ kpc. Solid line is the expected relation from Toomre's analysis, given by equation (2).

imations mentioned above, and the factor-of-two agreement is already interesting.

We can still test the expected increase of Q with the ratio $\lambda/\lambda_{\text{crit}}$. For this we recalculate the Q parameter and the wavelength λ_{crit} for a larger patch size of $L = 0.4$ kpc. The arrows in Figure 9 show the direction of change for both variables. Remarkably, they point in the direction expected from the linear theory.

The condition $Q < 1$ could be used to select star-forming regions. The gas mass in patches that satisfy this condition is $\sim (1-5.5) \times 10^8 M_\odot$, which generally accounts for 60-70% of the total H_2 mass (except for the weaker feedback run, which has less than 10% of the H_2 mass in $Q < 1$ patches). This mass is comparable to the mass converted to stars within 50 Myr. Except for SFE50-SNR3 run, the ratio of mass of young stars formed within 50 Myr to mass of H_2 in patches with $Q < 1$ varies between 0.34 and 3 for the different runs. Therefore, we can expect that most of the present molecular gas would be converted to stars on a timescale 50-100 Myr. This estimate is very approximate because Figure 7 shows that the star forming regions do not align with the unstable $Q < 1$ patches after 50 Myr. The match is better for very young star formation within only 10 Myr. In the next section we investigate the gas consumption timescale in detail, and consider different patch sizes and different ways of centering the search region.

4 GAS DEPLETION TIME

An important measure of the global efficiency of star formation in galaxies is the gas depletion time. For our patches of size L , we define it as the ratio of the molecular gas surface density to the surface density of star formation:

$$t_{\text{dep}}(L) = \frac{\Sigma_{H_2}(L)}{\Sigma_{\text{SFR}}(L)}. \quad (16)$$

Schruba et al. (2010), Feldmann et al. (2011), and Kruijssen & Longmore (2014) showed that the value of the depletion time depends on the spatial scale at which it is measured. It also depends on how the densities of gas and stars are calculated. In most observations they are counted in circular apertures centered on peaks of SFR density. Such regions may not already contain most of the gas they had before the onset of the star formation episode, resulting in relatively short depletion timescales. On the other hand, if the apertures are centered on peaks of the current gas density, the depletion times appear systematically longer.

To compare these two approaches, we use the following algorithm to calculate the surface densities of gas and SFR in patches of 100, 300, 500, and 1100 pc. First, we cover the plane of the galaxy with a rectangular grid of 100×100 cells, each 100 pc wide and ± 2 kpc thick, and calculate Σ_{H_2} and Σ_{SFR} in each cell. To go to larger size of 300 pc, we search for maximum of H_2 mass (or SFR), record the position of that peak, group the peak and its surrounding $3^2 - 1 = 8$ cells into a larger patch and sum the H_2 mass and SFR in this group. We label these 9 cells as "counted" and repeat the loop for the yet uncounted cells. Now we have a list of patches of 300 pc. Then we repeat this procedure for the chosen peaks and group 5^2 cell to obtain patches of 500 pc, etc.

Using this algorithm, we calculate the depletion time t_{dep} of H_2 gas in patches of different size from 100 pc to 1.1 kpc. The patches are chosen to be centered on peaks of H_2 mass or SFR. For the "centered-on-gas" version, we calculate the median of t_{dep} in patches with $M_{H_2} > 10^6 M_\odot$ to eliminate the low-density regions that would be unable to form stellar particles in our cluster formation algorithm, and count the SFR averaged over 50 Myr for better statistics. For the "centered-on-SFR" or "centered-on-young-stars" version (which we call "centered-on-stars" for brevity), we consider patches with any non-zero SFR, and count the SFR averaged over 10 Myr in order to approximate more closely the instantaneous star formation.

To show the full range of t_{dep} in both versions, in Figure 10 we plot the cumulative distribution of t_{dep} for patches of the smallest size (100 pc). In the "centered-on-gas" version (left panel), the cumulative distributions of t_{dep} weighted by H_2 mass do not reach 100%. This happens because some patches contain no stellar particles and therefore have formally infinite depletion time. The number of such patches is particularly large for SFE200 run, which has strongly misaligned molecular gas and young stars (see Figure 6). For the median H_2 mass the depletion time ranges between $10^{9.5}$ and $10^{10.5}$ yr in the strong-feedback runs.

In contrast, the right panel shows that the depletion time in the "centered-on-stars" version is significantly shorter, typically below 10^8 yr. Such discrepancy between the two counting methods is due to the gas-star misalignment which we emphasized above. Most of the star-forming

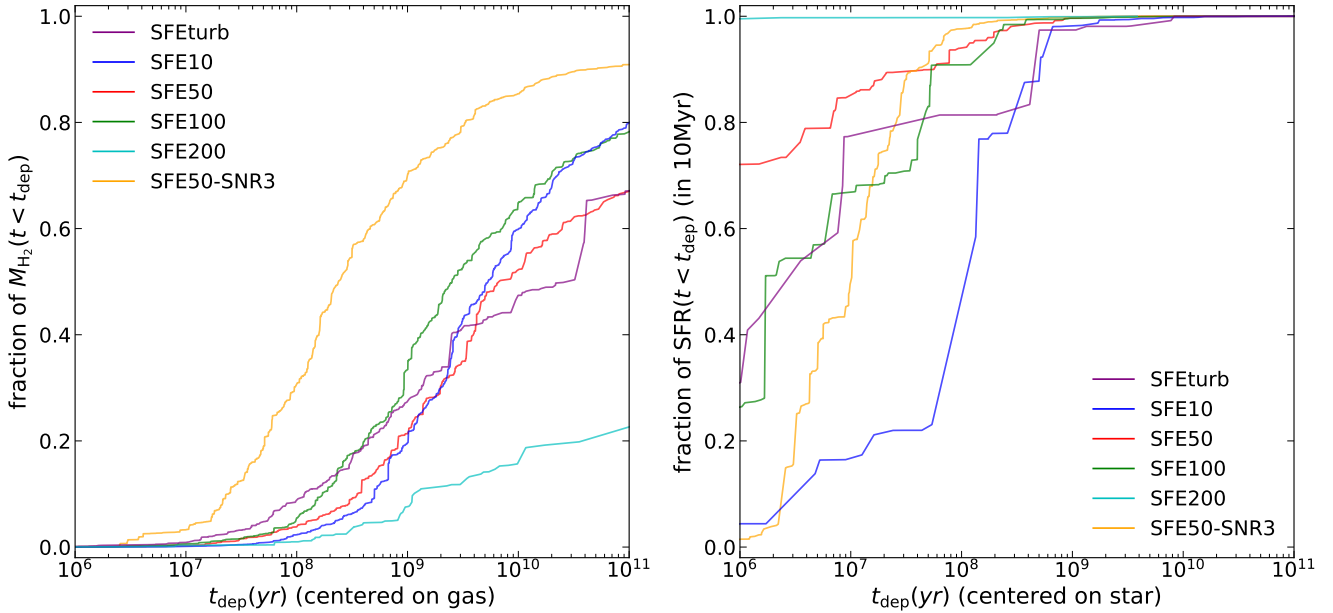


Figure 10. Cumulative distribution of the depletion time of molecular gas in patches of 100 pc in size. Left panel is for patches with $M_{\text{H}_2} > 10^6 M_{\odot}$ centered on gas density peaks, weighted by H_2 mass. Right panel is for patches with non-zero SFR within 10 Myr centered on SFR peaks, weighted by SFR.

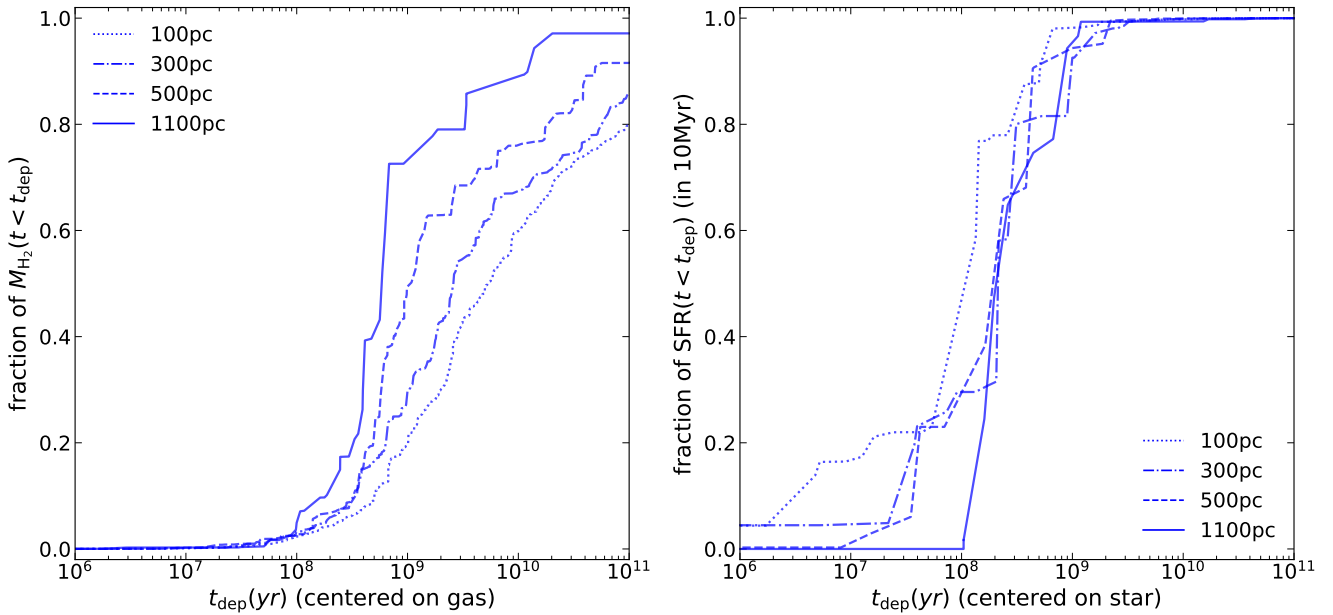


Figure 11. Cumulative distribution of H_2 depletion time for "centered-on-gas" (left panel) and "centered-on-stars" (right panel) versions for patches of different size. Here we show run SFE10 as an example. For "centered-on-gas" version, we use patches with $M_{\text{H}_2} > 10^6 M_{\odot}$ and weight them by H_2 mass. For "centered-on-stars" version, we use patches with non-zero SFR and weight them by SFR. As patch size increases, the distribution shifts to smaller t_{dep} for "centered-on-gas" case and to larger t_{dep} for "centered-on-stars" case, similarly to the trend shown in Figure 12.

sites have so little gas left within 100 pc that it would be exhausted in a relatively short interval of time.

Both versions of the gas depletion timescale vary strongly with the spatial scale on which they are calculated. To illustrate this dependence, we choose two representative runs (SFE50 and SFE10) and in Figure 11 we plot cumu-

lative distributions of t_{dep} for different patch sizes. The distribution of t_{dep} in the "centered-on-gas" version shifts to smaller values as patch size increases, by an order of magnitude between 100 pc and 700 pc. This shift is monotonic with the patch size and similar for the two runs shown.

The "centered-on-stars" version shows the opposite

trend: t_{dep} shifts to larger values. This change is roughly monotonic but differs between the two runs. In one case where t_{dep} was very short on 100 pc scale (SFE50) the increase is dramatic, by about two orders of magnitude. In the other case with larger t_{dep} (SFE10) the increase is only by a factor of two.

Adopting lower values of the threshold $M_{\text{H}_2} > 10^4 - 10^6 M_{\odot}$ increases the fraction of patches with infinite t_{dep} , leading to larger scatter in t_{dep} . If the threshold is taken to be $10^4 M_{\odot}$, even the median value of t_{dep} in SFE200 run is infinite for all patch sizes. In the other runs, the median value of t_{dep} changes within 0.5 dex for the smallest patch size, and correspondingly less for larger patch sizes. On the other hand, increasing the threshold mass greatly reduces the available number of patches, so we do not set the threshold above $10^6 M_{\odot}$.

Despite the above variations, the estimate of t_{dep} in both versions for all runs approaches a similar common range at the largest considered scale, $L = 1.1$ kpc. This convergence is illustrated in Figure 12. The median values over patches for different runs are all contained within $10^8 - 10^9$ yr. Unlike Figures 10 or 11, here the statistics of patches are not weighted by gas mass or SFR. The convergence is not strictly monotonic in all runs and there is large scatter from patch to patch. It is illustrated by shaded regions for one run; the amount of scatter is typical of all runs. In Section 5.2 we compare our results with the expectation of models of galactic star formation and available observational estimates.

The depletion times for gas-centered and star-centered patches do not match exactly on the largest scale, because we average the SFR over different timescales in the two cases: 50 Myr for gas-centered patches and 10 Myr for star-centered patches. The reason for using different timescales is that young stars and molecular gas coincide little in our simulations due to strong feedback. Averaging the SFR in 50 Myr for star-centered t_{dep} would lead to values smaller by several orders of magnitude.

We have also checked how the estimate of the depletion time varies with time, by examining previous outputs of each run. For the weaker feedback run SFE50-SNR3, the difference on all scales is small. For the other runs, the depletion time on kpc scale generally changes by factor of a few, while on smaller scales the difference is larger. The variation of t_{dep} is larger for "center-on-stars" patches than for "center-on-gas" patches, because the value of SFR over 10 Myr is more stochastic, leading to larger scatter in t_{dep} . Galaxies going through a merger show more divergent estimates of t_{dep} for both "center-on-gas" and "center-on-stars" versions on all scales, because of smaller overlap of SFR and molecular gas. The scatter of depletion time in previous outputs is similar to the scatter in snapshots shown in Figure 12.

4.1 Dependence of the depletion time on gas metallicity

We calculated the median values of the H_2 depletion time for patches of interest with metallicity higher and lower than the median metallicity. For almost all runs and all patch sizes, in both versions, the median t_{dep} of patches with high metallicity is smaller than that of patches with low metallicity. However, the whole metallicity distribution is contained to

a very narrow range (the interquartile range is smaller than $0.1 Z_{\odot}$ for all runs except SFE50-SNR3) such that the difference between the "high-metallicity" and "low-metallicity" values cannot be expected to lead to any substantial differences in physical properties of the gas. At the same time, the SFR density has a very large spread of several orders of magnitude in both cases. Therefore, we think that the dependence of t_{dep} on metallicity cannot be robustly determined with our data.

5 DISCUSSION

5.1 Toomre analysis

The Toomre Q parameter has been measured in several observational studies, at high and low redshift. Genzel et al. (2011) mapped four $z \approx 2$ star-forming galaxies in gaseous Q , including a correction for multiple components. They find that H_{α} clumps marking young stellar systems are present at the locations of gravitationally unstable gas ($Q \lesssim 1$). However, this correspondence could result from their indirect inference of the gas density by using the same H_{α} flux coupled with the global star formation relation. Follow-up work by Genzel et al. (2014) find values of $Q < 1$ in the outer regions of the observed galaxies and an increase towards the center, which they associate with higher central mass concentration and larger κ .

Romeo & Wiegert (2011) and Romeo & Falstad (2013) used their Q_2 and Q_3 definitions to calculate the Toomre parameter for a sample of nearby spiral galaxies from the THINGS survey of Leroy et al. (2008). They find values of $Q \approx 2 - 5$, and no strong trend with galactocentric radius. In one third of the galaxies Q is dominated by H_2 in the inner parts and in the rest it is dominated by stars at all radii. Westfall et al. (2014) used integral field spectroscopy for 27 nearby face-on spiral galaxies from Martinsson et al. (2013) to calculate Q_{RW} , which is equivalent to Q_2 but includes corrections for disk thickness (Romeo & Wiegert 2011). They find $Q \approx 1 - 3$, with some increase near the center due to rising κ_R . In two thirds of their galaxy sample, Q is dominated by the cold gas. Finally, Hitschfeld et al. (2009) estimate $Q \approx 2 - 4$ for the M51 galaxy, with smaller Q in spiral arms and in the outer disk. The total Q , calculated as a three-component sum assuming equal velocity dispersions, shows no obvious radial trend but the gaseous component Q_g alone increases towards the galaxy center.

In summary, observations of low-redshift galaxies indicate marginally stable disks, with occasional collapsing regions due to spiral arms or other gravitational perturbations. In contrast, high-redshift galaxies show more unstable regions and higher star formation rates. Our simulated galaxies resemble these high-redshift observations, however, we do not find the values of Q increasing towards the galaxy center. Our distribution of Q is very patchy, and in general Q increases towards the outer parts with low gas density.

Various numerical simulations of galaxy formation have also investigated the Toomre stability criterion. For isolated disk galaxies, Li et al. (2005) used the full Rafikov (2001) definition of the Q parameter, and found that the star-formation timescale increases exponentially with Q_R . Li et al. (2006) further found an anti-correlation between

the SFR and the minimum value of Q within the disk. This trend probably arises because both quantities depend on the gas density: $\text{SFR} \propto \Sigma$ and $Q_{\min} \propto \Sigma^{-1}$. Westfall et al. (2014) find a similar anti-correlation in their sample between the SFR surface density and Q_{\min} , although with large scatter. For our galaxies, the lowest value of Q in patches is not representative of all star formation, but we checked that the H_2 mass-weighted median value of Q does not correlate with the SFR.

In simulations of high-redshift ($z \approx 2.3$) galaxies, Ceverino et al. (2010) calculated a two-component Q and found unstable regions in spiral arms and dense clumps. More recently, Inoue et al. (2016) calculated the Q_2 parameter for their high-redshift clumpy disk galaxies after removing the bulge and treating stars younger than 100 Myr as a gas component. They found relatively high values $Q \gtrsim 2 - 3$ in interclump regions and $Q < 1$ only in very dense clumps. They also found that clumps begin forming with a high value of Q , which then decreases as clumps become denser. Such stable disks could be a consequence of high mass concentration and low gas density, resulting from insufficiently strong stellar feedback. We find similarly high Q values, low gas fraction, and high $\text{SFR} \gtrsim 10 M_{\odot} \text{ yr}^{-1}$ in our weak feedback SFR50-SNR3 run.

Analysis of the FIRE simulations presented in Oklopčić et al. (2017) has a very similar setup to ours: a 10 kpc square grid, with a 50 pc cell size smoothed to ~ 120 pc to identify stellar clumps. They calculate the gaseous parameter Q_g by approximating $\sigma = \sigma_z$ and $\kappa = \Omega$, and find that many gas clumps at the $z \approx 2$ output overlap with regions of $Q < 1$, but do not match exactly. This is similar to our results that low values of Q trace high-gas-density regions. We are also in agreement that the spatial coincidence between gas density peaks and SFR peaks washes out with increasing age of the stars.

To summarize our analysis of disk stability, we can ask: How well does the $Q < 1$ criterion work to predict the location and amount of star formation in these high-redshift galaxies? Is it a better criterion than a simple threshold on the H_2 density? We think the answer is yes.

The amount of H_2 currently contained within the contours enclosing 99% of SFR, averaged over 50 Myr, is similar to that in patches with $Q < 1$. However, when we look only at regions containing 99% of SFR within the shorter timescale of 10 Myr, the H_2 mass shows much more variation among the different runs (with the same stronger-feedback prescription): from 0.04 to 90 times the mass of stars formed in this period. Even if we select the very narrow part of the disk, calculating the column density of gas and SFR within only ± 0.2 kpc, the range of variation still extends from 0.3 to 38 times. In contrast, the H_2 mass selected by the $Q < 1$ criterion varies only between 5.5 and 220 times the young star mass. This shorter range of variation makes the Q criterion more useful for predicting future star formation.

Another way to make this comparison is to define a threshold in H_2 surface density such that the mass contained in patches above that threshold matches the mass in patches with $Q < 1$. We find that this threshold would vary from 48 to $110 M_{\odot} \text{ pc}^{-2}$ for the different strong-feedback runs, that is, by more than factor of two. For $\text{HI} + \text{H}_2$ gas the corresponding thresholds would be even higher: $140 - 250 M_{\odot} \text{ pc}^{-2}$. (For the weak-feedback run the thresholds are another order of

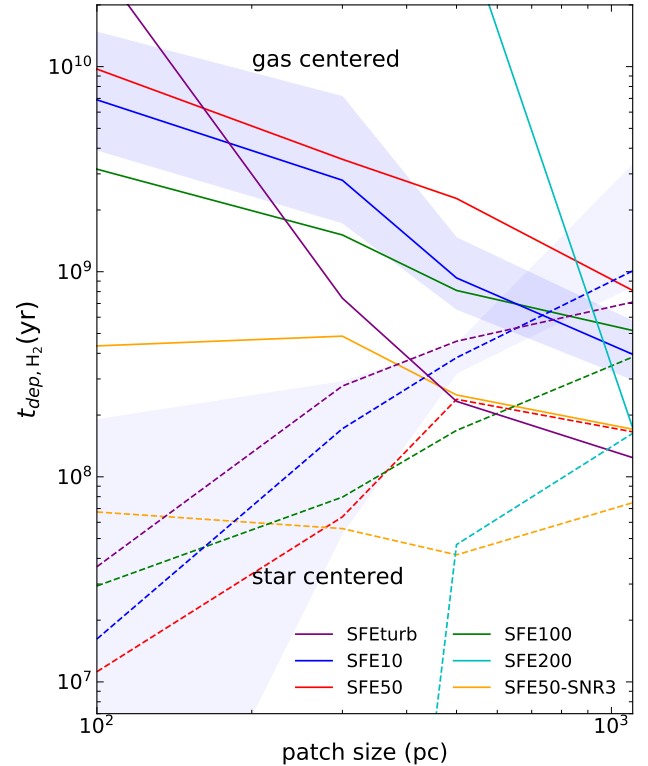


Figure 12. Depletion time of H_2 for "centered-on-gas" (solid lines) and "centered-on-stars" versions (dashed lines) as a function of patch size. For "centered-on-gas" version, we take the median of t_{dep} in patches with $M_{\text{H}_2} > 10^6 M_{\odot}$. For "centered-on-stars" version, we take the median of t_{dep} in patches with non-zero SFR. Shaded regions show the 40%-60% range of the values of t_{dep} for SFE10 run, to illustrate the typical wide spread of the distribution.

magnitude larger.) These densities significantly exceed the prediction of Schaye (2004) model, in which transition to star-forming gas in present-day galaxies is expected to happen at $3 - 10 M_{\odot} \text{ pc}^{-2}$. This may be an evidence for denser and more compact ISM in galaxies at $z \approx 1 - 2$.

5.2 Depletion time

Utomo et al. (2017) and Colombo et al. (2018) measured the depletion time of molecular gas on kpc scale in the EDGE-CALIFA survey of nearby galaxies. They found $t_{\text{dep}} \approx 2.4$ Gyr, with large scatter of about 0.5 dex. The depletion time decreases near the center in some of the galaxies, especially at lowest masses $M_* \lesssim 10^{10} M_{\odot}$.

For high-redshift galaxies the depletion time of molecular gas appears to be shorter. According to Genzel et al. (2010), the depletion time for normal star-forming galaxies decreases from 1.5 Gyr at $z \approx 0$ to 0.5 Gyr at $z \approx 2$. Tacconi et al. (2010, 2013) measured $t_{\text{dep}} \approx 0.7$ Gyr, with a dispersion of 0.24 dex, in a survey of $z \approx 1 - 3$ galaxies with $M_* > 2.5 \times 10^{10} M_{\odot}$ and $\text{SFR} \gtrsim 30 M_{\odot} \text{ yr}^{-1}$. However, it is important to note the large scatter associated with this mean trend – a small selection of galaxies may deviate significantly. For example, Tadaki et al. (2018) find a very short depletion time of 10^8 yr in a sub-mm starburst galaxy at

$z = 4.3$. This galaxy shows giant kpc-scale molecular gas clumps with low $Q \approx 0.3$, due to the very high gas density. [Forrest et al. \(2018\)](#) also find spread of two orders of magnitude for the specific SFR of $1 < z < 4$ galaxies in the large ZFOURGE survey.

Our simulated galaxies, except in the weaker feedback SFE50-SNR3 run and the higher-redshift SFETurb output, show comparable values of t_{dep} to the observations of $z \approx 1-2$ galaxies. When averaged in cylindrical shells, the depletion time roughly follows the trend of decreasing towards the center but given the strong patch-to-patch variation we do not study it further.

Recent observations by [Rebolledo et al. \(2015\)](#) and [Leroy et al. \(2017\)](#) have been able to probe individual star-forming regions on scales below 100 pc in nearby galaxies. They reveal a wide scatter of SFR density by three orders of magnitude at H_2 densities $10 - 10^3 M_{\odot} \text{ pc}^{-2}$. Our simulations show a correspondingly large scatter in the local depletion times. Taking the patches above our adopted threshold on the H_2 mass, which corresponds to the surface density of $10^6 M_{\odot} / (200 \text{ pc})^2 = 25 M_{\odot} \text{ pc}^{-2}$, we find few individual patches with $t_{\text{dep}} < 10^8 \text{ yr}$ in the stronger-feedback runs. This corresponds to the lowest bound derived by [Rebolledo et al. \(2015\)](#). We find some patches with $t_{\text{dep}} > 10^{10} \text{ yr}$, which fall above the observed upper limit. However, such regions are more likely to escape detection because of their lower SFR. There is no systematic trend with ϵ_{ff} used in the simulation. Also, as with most of our results, the weaker-feedback run is an exception, as it contains patches with the depletion times as short as 10^7 yr .

The high-redshift galaxies appear to have a high molecular gas fraction: [Tacconi et al. \(2013\)](#) measured $f_{\text{mol}} = M_{\text{mol}} / (M_{\text{mol}} + M_{*}) \sim 50\%$. After correcting for incompleteness, f_{mol} lowers to $30 - 40\%$. That fraction is larger than what we find for our simulated galaxies (about 15%), even though our galaxies are less massive and therefore should be more gas-rich. [Daddi et al. \(2010\)](#) also found the molecular gas fraction of galaxies at $z \approx 1.5$ to be $\sim 50 - 65\%$. At very high redshift, the molecular gas fraction is even larger: [Dessauges-Zavadsky et al. \(2017\)](#) measured $f_{\text{mol}} \approx 60 - 79\%$ for a lensed $M_{*} \sim 5 \times 10^9 M_{\odot}$ galaxy at $z \approx 3.6$. In our galaxies the fraction of neutral gas reaches about 50%, but the fraction of molecular gas stays low regardless of the value of local star formation efficiency adopted in the simulation (see Table 1).

Theoretical models predict the scaling of the depletion time with properties of star-forming regions. [Semenov et al. \(2017\)](#) constructed an analytical model based on the mass conservation and the physical picture of rapid gas evolution between star-forming and non-star-forming states to study t_{dep} and the fraction of gas that participates in star formation. They tested this model with a suite of L_{*} -sized galaxy simulations ([Semenov et al. 2018](#)) with different values of ϵ_{ff} , feedback strength f_{boost} (b in their notation), and star formation threshold. According to their model, gas regulation in galaxies is divided into two regimes: the self-regulation regime where feedback is strong or ϵ_{ff} is large enough, and the dynamics-regulation regime where feedback is weak or ϵ_{ff} is small. In the dynamics-regulation regime, the supply of star-forming gas is balanced by dispersal due to dynamical processes such as turbulent shear, differential rotation, etc. The depletion time is inversely proportional to ϵ_{ff} , and

the star-forming gas fraction is insensitive to ϵ_{ff} or feedback strength. In the self-regulation regime, gas spends most of the time in non-star-forming stages, and gas regulation is mainly controlled by star formation and feedback. The depletion time scales with feedback strength, but is insensitive to ϵ_{ff} . The star-forming gas fraction is small and scales inversely with f_{boost} and ϵ_{ff} . Although the model is formulated for the depletion time of all gas on kpc scales, the behavior of $t_{\text{dep}, \text{H}_2}$ and H_2 fraction with different ϵ_{ff} and feedback strength is similar.

Our simulated galaxies fall in the self-regulation regime. Consistent with the [Semenov et al. \(2017\)](#) model, our $t_{\text{dep}, \text{H}_2}$ on the largest scale shows a slightly decreasing trend with ϵ_{ff} , although non-monotonic and with large scatter. It may be mainly due to the fraction of gas in molecular phase, $M_{\text{H}_2} / M_{\text{HI} + \text{H}_2}$, generally falling with ϵ_{ff} . The weaker feedback run has slightly smaller $t_{\text{dep}, \text{H}_2}$ and higher H_2 fraction than the other runs, which is also consistent with their model. The scale dependence of t_{dep} is also similar, but our results are less regular and show significant scatter.

Galactic star formation relations are expected to break down below a certain spatial scale due to incomplete sampling of star formation or gas tracers, and relative motion of dense gas and young stars because of stellar feedback. The scatter of star formation relations, coming from the discreteness and stochasticity of star formation, and drifting of young stars, becomes more significant on smaller scales ([Feldmann et al. 2011, 2012](#)). [Kruijssen & Longmore \(2014\)](#) constructed a model to describe this breakdown of SF relations based on the concept that a galaxy consists of many independent star-forming regions separated by some length scale, and that these regions are going through the SF process during which gas and/or young stars can be observed by some tracer. The timescale of the whole SF process is a combination of the epoch when gas is visible (t_{gas}) and when stars are visible (t_{star}), with some overlap time (t_{over}). The scatter in t_{dep} increases from ~ 0.1 dex on kpc scale to ~ 1 dex on tens of pc scale for randomly positioned apertures. Centering apertures on gas or stellar peaks systematically biases t_{dep} – centering on gas peaks overestimates t_{dep} and centering on stellar peaks underestimates t_{dep} – making the “tuning fork” diagram, as shown in our Figure 12. The relative durations of the various phases of SF process ultimately determine the excess or deficit of t_{dep} on small scales.

[Kruijssen et al. \(2018\)](#) provide a detailed method to reconstruct the timescales of star formation and feedback (t_{gas} , t_{star} , t_{over}) from the maps of gas and stellar flux. Using their method requires that the SFR for both gas-centered and star-centered apertures is averaged over the same time span. We find the ratio of the gas-centered to star-centered t_{dep} about a factor of 100 at the smallest scale of 100 pc, with a very large variation between the different runs; these numbers exceed even the largest expected spread shown in [Kruijssen et al. \(2018\)](#). From our Figure 12 we can at least see that our t_{gas} is much larger than t_{star} (taken to be 10 Myr here). From Figure 6 we can infer that our t_{over} is definitely smaller than 50 Myr, and probably close to 10 Myr, which explains why we have so many infinities in the gas-centered determination of t_{dep} . The depletion time is so short on small scales when centered on stars that dense gas does not coincide with young stars, and causes formally infinite t_{dep} .

6 SUMMARY

We have investigated the structure of high-redshift ($z \approx 1.5 - 2$) galaxies in a suite of cosmological simulations with different star formation efficiency and feedback strength. Our main results are summarized below:

- Unlike the regular appearance of low-redshift disk galaxies, the galaxies in our simulations have thick stellar disks with irregular, prolate shapes. The kinematics are dominated by turbulent motions and not by rotation. The stellar surface density profiles are approximately exponential, with the scale length of about 1 kpc.
- Although the vertical scale heights for all gas and all stars are large, cold molecular gas is concentrated in relatively thin disks. Young stars, which form from the molecular gas, likewise have the distribution with axis ratios $c/a = 0.1 - 0.2$.
- Spatial correlation between the peaks of gas density and SFR deteriorates with the age of stellar population and almost disappears after ~ 50 Myr, because of stellar feedback dispersing old gas clouds around star-forming regions.
- We calculate the maps of Toomre Q parameter in patches of 200 pc, combining three components with different velocity dispersions: stars, molecular gas, and atomic gas. The median value of Q weighted by H_2 mass is in the range 0.5 – 1, surprisingly close to unity given the irregular structure of the galaxies.
- The median value weighted by neural $HI + H_2$ mass is higher: $Q \approx 1.5 - 2.6$. The Q parameter in the weaker feedback run SFE50-SNR3 is systematically larger than in the other runs, because of the low gas density and high central mass concentration.
- The dynamic range of Q maps is much smaller than that of the H_2 surface density maps, making the Toomre Q parameter a better indicator of unstable regions that would collapse and form stars. The Q parameter also depends on the spatial scale over which it is calculated: enlarging the averaging scale increases the value of Q .
- The depletion time of molecular gas in our galaxies is around 1 Gyr on the kpc scale, with large scatter from run to run. On smaller scales, t_{dep} splits to systematically larger or smaller values when centering the aperture on gas peaks or stellar peaks, respectively.

ACKNOWLEDGEMENTS

We thank Miroslava Dessauges-Zavadsky, Andrey Kravtsov, Nir Mandelker, Roman Rafikov, and Vadim Semenov for useful discussions. This work was supported in part by NSF through grant 1412144.

REFERENCES

Binney J., Tremaine S., 2008, Galactic Dynamics. Princeton, NJ: Princeton Univ. Press

Brown G., Gnedin O. Y., Li H., 2018, *ApJ*, **864**, 94

Ceverino D., Dekel A., Bournaud F., 2010, *MNRAS*, **404**, 2151

Ceverino D., Primack J., Dekel A., 2015, *MNRAS*, **453**, 408

Colombo D., et al., 2018, *MNRAS*, **475**, 1791

Daddi E., et al., 2010, *ApJ*, **713**, 686

Dekel A., Sari R., Ceverino D., 2009, *ApJ*, **703**, 785

Dessauges-Zavadsky M., et al., 2017, *A&A*, **605**, A81

Diesing R., Caprioli D., 2018, *Physical Review Letters*, **121**, 091101

Elmegreen D. M., Elmegreen B. G., 2014, *ApJ*, **781**, 11

Elmegreen B. G., Elmegreen D. M., Tompkins B., Jenks L. G., 2017, *ApJ*, **847**, 14

Feldmann R., Gnedin N. Y., Kravtsov A. V., 2011, *ApJ*, **732**, 115

Feldmann R., Gnedin N. Y., Kravtsov A. V., 2012, *ApJ*, **758**, 127

Fisher D. B., et al., 2017, *MNRAS*, **464**, 491

Forrest B., et al., 2018, *ApJ*, **863**, 131

Garrison-Kimmel S., et al., 2018, *MNRAS*, submitted; arXiv:1712.03966

Genzel R., et al., 2010, *MNRAS*, **407**, 2091

Genzel R., et al., 2011, *ApJ*, **733**, 101

Genzel R., et al., 2014, *ApJ*, **785**, 75

Gnedin N. Y., 2014, *ApJ*, **793**, 29

Gnedin N. Y., Abel T., 2001, *NewA*, **6**, 437

Gnedin N. Y., Kravtsov A. V., 2011, *ApJ*, **728**, 88

Haardt F., Madau P., 2001, *p. 64*

Hitschfeld M., Kramer C., Schuster K. F., Garcia-Burillo S., Stutzki J., 2009, *A&A*, **495**, 795

Inoue S., Dekel A., Mandelker N., Ceverino D., Bournaud F., Primack J., 2016, *MNRAS*, **456**, 2052

Kravtsov A. V., 1999, PhD thesis, NEW MEXICO STATE UNIVERSITY

Kravtsov A. V., 2003, *ApJ*, **590**, L1

Kravtsov A. V., Klypin A. A., Khokhlov A. M., 1997, *ApJS*, **111**, 73

Kruijssen J. M. D., Longmore S. N., 2014, *MNRAS*, **439**, 3239

Kruijssen J. M. D., Schruba A., Hygate A. P. S., Hu C.-Y., Haydon D. T., Longmore S. N., 2018, *MNRAS*,

Krumholz M. R., Burkhardt B., Forbes J. C., Crocker R. M., 2018, *MNRAS*, **477**, 2716

Leroy A. K., Walter F., Brinks E., Bigiel F., de Blok W. J. G., Madore B., Thornley M. D., 2008, *AJ*, **136**, 2782

Leroy A. K., et al., 2017, *ApJ*, **846**, 71

Li Y., Mac Low M.-M., Klessen R. S., 2005, *ApJ*, **626**, 823

Li Y., Mac Low M.-M., Klessen R. S., 2006, *ApJ*, **639**, 879

Li H., Gnedin O. Y., Gnedin N. Y., Meng X., Semenov V. A., Kravtsov A. V., 2017, *ApJ*, **834**, 69

Li H., Gnedin O. Y., Gnedin N. Y., 2018, *ApJ*, **861**, 107

Martinsson T. P. K., Verheijen M. A. W., Westfall K. B., Bershady M. A., Schechtman-Rook A., Andersen D. R., Swaters R. A., 2013, *A&A*, **557**, A130

Martizzi D., Faucher-Giguère C.-A., Quataert E., 2015, *MNRAS*, **450**, 504

Nelson A. F., 2006, *MNRAS*, **373**, 1039

Oklopčić A., Hopkins P. F., Feldmann R., Kereš D., Faucher-Giguère C.-A., Murray N., 2017, *MNRAS*, **465**, 952

Orr M. E., et al., 2018, *MNRAS*, submitted,

Papovich C., et al., 2015, *ApJ*, **803**, 26

Pfeffer J., Kruijssen J. M. D., Crain R. A., Bastian N., 2018, *MNRAS*, **475**, 4309

Rafikov R. R., 2001, *MNRAS*, **323**, 445

Rebolledo D., Wong T., Xue R., Leroy A., Koda J., Donovan Meyer J., 2015, *ApJ*, **808**, 99

Reina-Campos M., Kruijssen J. M. D., 2017, *MNRAS*, **469**, 1282

Romeo A. B., Falstad N., 2013, *MNRAS*, **433**, 1389

Romeo A. B., Wiegert J., 2011, *MNRAS*, **416**, 1191

Rudd D. H., Zentner A. R., Kravtsov A. V., 2008, *ApJ*, **672**, 19

Safronov V. S., 1960, *Annales d'Astrophysique*, **23**, 979

Schaye J., 2004, *ApJ*, **609**, 667

Schmidt W., et al., 2014, *MNRAS*, **440**, 3051

Schruba A., Leroy A. K., Walter F., Sandstrom K., Rosolowsky E., 2010, *ApJ*, **722**, 1699

Semenov V. A., Kravtsov A. V., Gnedin N. Y., 2016, *ApJ*, **826**, 200

Semenov V. A., Kravtsov A. V., Gnedin N. Y., 2017, [ApJ](#), **845**, 133

Semenov V. A., Kravtsov A. V., Gnedin N. Y., 2018, [ApJ](#), **861**, 4

Shibuya T., Ouchi M., Kubo M., Harikane Y., 2016, [ApJ](#), **821**, 72

Tacconi L. J., et al., 2010, [Nature](#), **463**, 781

Tacconi L. J., et al., 2013, [ApJ](#), **768**, 74

Tadaki K., et al., 2018, [Nature](#), **560**, 613

Tamburello V., Mayer L., Shen S., Wadsley J., 2015, [MNRAS](#), **453**, 2490

Tomassetti M., et al., 2016, [MNRAS](#), **458**, 4477

Toomre A., 1964, [ApJ](#), **139**, 1217

Toomre A., 1977, [ARA&A](#), **15**, 437

Utomo D., et al., 2017, [ApJ](#), **849**, 26

Vollmer B., Leroy A. K., 2011, [AJ](#), **141**, 24

Westfall K. B., Andersen D. R., Bershady M. A., Martinsson T. P. K., Swaters R. A., Verheijen M. A. W., 2014, [ApJ](#), **785**, 43

Zemp M., Gnedin O. Y., Gnedin N. Y., Kravtsov A. V., 2011, [ApJS](#), **197**, 30

Zhang H., et al., 2018, preprint, ([arXiv:1805.12331](#))

van der Wel A., et al., 2014, [ApJ](#), **792**, L6

This paper has been typeset from a \TeX / \LaTeX file prepared by the author.